



저작자표시-비영리-변경금지 2.0 대한민국

이용자는 아래의 조건을 따르는 경우에 한하여 자유롭게

- 이 저작물을 복제, 배포, 전송, 전시, 공연 및 방송할 수 있습니다.

다음과 같은 조건을 따라야 합니다:



저작자표시. 귀하는 원저작자를 표시하여야 합니다.



비영리. 귀하는 이 저작물을 영리 목적으로 이용할 수 없습니다.



변경금지. 귀하는 이 저작물을 개작, 변형 또는 가공할 수 없습니다.

- 귀하는, 이 저작물의 재이용이나 배포의 경우, 이 저작물에 적용된 이용허락조건을 명확하게 나타내어야 합니다.
- 저작권자로부터 별도의 허가를 받으면 이러한 조건들은 적용되지 않습니다.

저작권법에 따른 이용자의 권리는 위의 내용에 의하여 영향을 받지 않습니다.

이것은 [이용허락규약\(Legal Code\)](#)을 이해하기 쉽게 요약한 것입니다.

[Disclaimer](#)

공학박사학위논문

Nanoindentation Pop-in Behaviors in Steel

철강의 나노인덴테이션 시 나타나는 pop-in 현상 분석

2013년 2월

서울대학교 대학원

재료공학부

안 태 홍

NANOINDENTATION POP-IN BEHAVIORS IN STEEL

철강의 나노인덴테이션 시 나타나는 pop-in 현상 분석

지도교수 한 흥 남

이 논문을 공학박사학위논문으로 제출함
2012년 12월

서울대학교 대학원
재료공학부
안 태 홍

안태홍의 박사학위논문을 인준함
2012년 12월

위	원	장	<u>오 규 환</u> (인)
부	위	원	<u>한 흥 남</u> (인)
위		원	<u>박 은 수</u> (인)
위		원	<u>장 재 일</u> (인)
위		원	<u>최 인 석</u> (인)

ABSTRACT

Recently, nanoindentation has been employed to probe the small-scale mechanical behavior of materials for a wide range of academic or engineering applications. The response of a material to the nanoindentation is usually represented as a form of the load-displacement curve. When metallic materials undergo irreversible permanent deformation, the discrete physical events, such as dislocation nucleation, dislocation source activation, phase transformation or mechanically-induced twinning, can be detected as discontinuities of displacement or load during nanoindentation. These can produce geometrical softening accompanied by a sudden displacement excursion during load-controlled nanoindentation, which referred to in the literature as a pop-in. In this study, several physical events which cause pop-ins during nanoindentation of steel will be reported and discussed.

First, experimental results of nanoindentation and microstructural studies of metastable austenite in TRIP steel is reported to provide its micromechanical insight into the strain-induced phase transformation and deformation behavior. Sequential experiments were carried out, first using electron backscattered diffraction (EBSD) to map the phase and orientation distributions of the grains, followed by nanoindentation of individual austenite grains in the mapped region, then sectioning through an indent using focused

ion beam (FIB) milling and finally transmission electron microscopy (TEM) to confirm the formation of martensite from austenite under the indent. The load-displacement curve obtained from nanoindentation revealed two types of pop-in events on the loading segment. The first type was attributed to the elastic-to-plastic transition of austenite based on a Hertzian analysis of the elastic portion of the load-displacement curve. A second type of pop-in can be described as resulting from geometrical softening due to the selection of a favorable martensite variant based on the mechanical interaction energy between the externally applied stress and lattice deformation during nanoindentation. The existence of martensite after nanoindentation was confirmed by TEM analysis of the cross-section of an indented sample. The TRIP strain calculated by simple considering of crystal geometry change during phase transformation was in good agreement with the measured pop-in depth. Multiple pop-ins in less stable austenite was considered as a result of sequentially transformed multiple martensite from austenite.

Second, nanoindentation and microstructural studies are reported to provide experimental evidence of the relationship between the formation of ϵ martensite and pop-in behavior in metastable austenite in high nitrogen TRIP steel. Sequential experiments of EBSD, SPM, nanoindenter, FIB, and high resolution TEM (HR-TEM) were also carried out in order to directly observe ϵ martensite under the indent. The load-displacement curve obtained from nanoindentation revealed stepwise pop-ins in the early stage of plastic

deformation. Considering that the stress-induced ϵ martensite transformation is the predominant deformation mode in the early stage of plastic deformation and its monopartial nature as well, geometrical softening can also occur by ϵ martensite formation. From analyses of high resolution TEM images, a cluster of banded structure under the indent turned out a juxtaposition of (111) planes of γ austenite and (0001) planes of ϵ martensite. The most favorable slip system predicted by simple calculations based on the Schmid's law was the same one that experimentally observed by TEM. It was also calculated that formation of more than just 10 single ϵ martensite layers in this slip system can introduce several nanometers of pop-in. These microstructural investigations strongly suggest that the pop-in behavior in the early stage of plastic deformation of austenite is closely related to the formation of ϵ martensite.

Lastly, pop-ins on nanoindentation load–displacement curves of a ferritic steel were correlated with yield drops on its tensile stress–strain curves. To investigate the relationship between these two phenomena, nanoindentation and tensile tests were performed on annealed specimens, prestrained specimens, and specimens aged for various times after prestraining. Clear nanoindentation pop-ins were observed on annealed specimens, which disappeared when specimens were indented right after the prestrain, but reappeared to varying degrees after strain aging. Yield drops in tensile tests showed similar disappearance and appearance, indicating that the two

phenomena, at the nano- and macroscale, respectively, are closely related and influenced by dislocation locking by solutes (Cottrell atmospheres).

Keywords: Nanoindentation, Pop-in, Geometrical softening, Strain-induced martensitic transformation, ϵ martensite, Metastable austenite, TRIP steel, Yield point phenomena, Yield drop, Cottrell atmosphere, Nanoindenter, Electron BackScattered Diffraction (EBSD), Scanning Probe Microscopy (SPM), Focused Ion Beam (FIB), Transmission Electron Microscopy (TEM)

Student number: 2007-20720

Contents

Abstract	I
Table of Contents	V
List of Tables	IX
List of Figures	X

Chapter 1

Introduction

1. 1. Nanoindentation	1
1.1.1. Nanoindentation system	3
1.1.2. Displacement measurement	3
1.1.3. Force measurement	4
1. 2. Pop-in behavior during nanoindentation	8
1. 3. Hertzian elastic contact theory	12
1. 4. Thesis motivations	17

1. 5. References	19
-------------------------------	----

Chapter 2

Investigation of strain-induced martensitic transformation ($\gamma \rightarrow \alpha'$) in metastable Austenite

2. 1. Introduction	25
2. 2. Experimental procedures	28
2.2.1. Sample preparation	28
2.2.2. Measuring procedure	29
2. 3. Results and discussion	36
2. 4. Appendix: Surface control for multiphase steel	59
2. 5. Conclusions	68
2. 6. References	69

Chapter 3

Relationship between ϵ martensite formation ($\gamma \rightarrow \epsilon$) and pop-in behavior in high nitrogen steel

3. 1. Introduction	73
3.1.1. ϵ martensite in steel	73
3.1.2. Stacking fault energy & deformation microstructure in high N steel	75
3.1.3. Motivations and objectives	76
3. 2. Experimental procedures	79
3.2.1. Sample preparation	79
3.2.2. Measuring procedure	79
3.2.3. Determination of rotation angle in FIB	80
3. 3. Results and discussion	85
3. 4. Conclusions	98
3. 5. References	99

Chapter 4

Relationship between yield drop and nanoindentation

pop-in behavior of steel

4. 1. Introduction	102
4. 2. Experimental procedures	106
4. 3. Results and discussion	110
4. 4. Conclusions	123
4. 5. References	124

Chapter 5

General conclusions	129
----------------------------------	-----

LIST OF TABLES

Table 2.1. The 24 variants of K-S relation.

Table 2.2. The measured and calculated K-S variants for each martensite under the indent. Top 4 favorable variants out of 24 from mechanical interaction energy calculation were listed in the table.

Table 3.1. Schmid factor and the unit displacement along indentation axis, d_i , for 12 variants of Shockley partial movement.

Table 4.1. Maximum shear stress at pop-in in ($\tau_{\text{pop-in}}$) for annealed, pre-strained and strain aged conditions. No distinct pop-in was observed on pre-strained specimen.

LIST OF FIGURES

Figure 1.1. Schematic of typical load-displacement curve during loading-unloading cycle where h_{\max} is the maximum indenter displacement at peak indentation load P_{\max} , and S is the contact stiffness (after Oliver and Pharr).

Figure 1.2. The nanoindentation system used in this study, TriboLab[®] 750Ubi, Hysitron

Figure 1.4. Example of “pop-in” event obtained during nanoindentation of an elastic-plastic material, in this case single crystal Cr_3Si (110).

Figure 1.5. Schematic of contact between a rigid indenter and a flat specimen with modulus E . The radius of the circle of contact is a , and the total depth of penetration is h_{\max} . h_a is the depth of the circle of contact from the specimen free surface, and h_c is the distance from the bottom of the contact to the contact circle (the contact depth).

Figure 2.1. A graphical plot (often called “a banana curve”) that shows change in total elongation as a function of yield strength for various steel products. The strength-ductility balance (tensile strength \times elongation) is often used as an index for mechanical characteristics or efficiency of steel products.

Figure 2.2. Temperature history of the steel for reverse transformation. The specimens were batch annealed.

Figure 2.3. Microstructure change upon reverse transformation.

Figure 2.4. Microstructure of the sample. (a) SEM image, (b) EBSD phase map. Red grains are FCC austenite and blue are BCC ferrite.

Figure 2.5. (a) EBSD phase map (Red: FCC, Blue: BCC), (b) orientation map of sample surface before indentation, (c) SPM image of indent in metastable austenite grain (yellow circle) and (d) Dotted yellow lines on SEM image showing schematically where FIB milling was used to cut out a cross-section through the indent for TEM analysis.

Figure 2.6. Sequential experiment procedures for measuring martensitic transformation from metastable austenite.

Figure 2.7. Comparison of experimental measurements (black symbols) to prediction of the Hertzian elastic load-displacement behavior (blue dashed line) of the metastable austenite grain shown in Figure 2.5. Arrows indicate the starting points of the three pop-ins.

Figure 2.8. (a) A typical image of Berkovich indenter. (b) A schematic of the

idealization of the indenter tip as a sphere.

Figure 2.9. Schematic diagram showing the geometry of the nanoindentation test with spherical indenters. Dislocations are idealized as a two dimensional square array with a spacing l .

Figure 2.10. (a) Bright field TEM image of the cross-section of a sample indented to a depth slightly beyond the third pop-in of Figure 2. Diffraction patterns from (b) region closest to the ferrite grain in (a) showing that it remains as austenite, γ and (c) region closest to the indenter in (a) showing that it has transformed to martensite, α' .

Figure 2.11. Schematic diagrams for Bain distortion. (a) Movement of crystal lattices for FCC-to-BCT transformation. Two tensile axes and one compressive axis are indicated. (b), (c) and (d) three different Bain variants depending on the direction of the compression axis. The variant whose compression axis for the Bain distortion is nearly parallel to the externally applied stress, σ_{ij} , has a higher probability of selection.

Figure 2.12. An FEM simulation for the von Mises stress and strain distribution underneath the indenter. Compressive stress along indentation axis, z , is dominant.

Figure 2.13. A schematic of crystal orientation and geometry with a cross-section TEM image underneath the indentation.

Figure 2.14. A load-displacement curve of a less stable austenite grain. The frequency of pop-in in a curve during plastic deformation was higher, compared to the steel in Figure 2.7.

Figure 2.15. (a) A TEM plan-view, (b) a phase map (Skyblue: BCC(BCT), Peach: FCC), (c) an orientation map measured by automatic TEM measuring system.

Figure 2.16. A computational simulation for the Cauchy stress distribution underneath the indenter using CP-FEM. The orientation which were measured by EBSD was used in the calculation.

Figure 3.1. Examples of different dislocations stackings: (a) self-accommodated stacking, (b) monopartial stacking.

Figure 3.2. Relationship between stacking fault energy and interstitial contents. The steel used in this study with 0.3wt% nitrogen content corresponds to stacking faults of about $15\text{mJ}\cdot\text{m}^{-2}$.

Figure 3.3. (a) EBSD phase map (Red: FCC, Blue: BCC), (b) orientation map

of sample surface before indentation, (c) SPM image of indent in metastable austenite grain. Dotted yellow lines on SPM image showing schematically where FIB milling was used to cut out a cross-section through the indent for TEM analysis. (d) An FIBed cross-section sample is attached to a Mo half-grid for TEM.

Figure 3.4. A schematic representation of the formation of monopartial ϵ martensite.

Figure 3.5. Microstructure change in austenite as tensile deformation increases.

Figure 3.6. Load-displacement curve obtained by nanoindentation of the metastable austenite grain.

Figure 3.7. A plan-view image of the cross-section sample, there is an obvious indent on the surface and deformed regions under the indent.

Figure 3.8. Diffraction patterns obtained around region A in Figure 3.6. Both (a) $\langle 111 \rangle \alpha'$ and (b) $\langle 110 \rangle \gamma$ were found in region A.

Figure 3.9. (a) A high resolution image of region B (zone= $[\bar{1}10]_{\gamma}$). (b) A closer look of (a). The image was rotated 15° in clockwise for easier view of

the lattices. (c) A numerical diffractogram obtained by FFT of (a).

Figure 4.1. A schematic of Cottrell atmosphere and corresponding tensile behaviors.

Figure 4.2. Strain aging. (a) Load removed from specimen at point *c* and specimen reloaded within a short period of time (hours). (b) Load removed at point *c* and specimen reloaded after a long period of time (months).

Figure 4.3. Microstructure of the ferritic steel by an optical microscope. (a) $\times 200$, (b) $\times 500$.

Figure 4.4. (a) A combined EBSD band contrast and slope map and (b) an SPM image for the fully annealed steel specimen showing majority ferrite grains, isolated ($\sim 1\%$) pearlite colonies, and an 8×8 array of indentations. Only those indents that were located squarely within the ferrite grains and away from the boundaries were analyzed in the present study.

Figure 4.5. Comparison of the uniaxial tensile stress-strain curves for the annealed steel specimen (arrows) with those obtained after (a) loading to 6% strain, unloading, and then immediately reloading and (b) loading to 6% strain, unloading, strain aging for 30 hours, and then reloading. The curves in (b) are offset from the origin for clarity of presentation.

Figure 4.6. Nanoindentation load-displacement curves obtained (a) before, (b) right after, (c) 30 hours after and (d) 3 weeks after 6% tensile pre-strain. In (a), (c) and (d) the experimental data (black lines) before the pop-ins match well the theoretical Hertzian elastic contact solution (blue dashed lines). In (b) the deformation is elastic-plastic practically right from the start.

Figure 4.7. A linear relation between the pop-in load and the amount of pop-in.

Figure 4.8. (a) An orientation map (ND) and (b) a corresponding Taylor factor map.

Figure 4.9. (a) Relationship between Taylor factor and the pop-in start load. (b) Distribution of pop-in start load in one grain.

Figure 4.10. Nanoindentation pop-in stresses before, right after, 30 hours after, and 3 weeks after the 6% tensile prestrain.

Chapter 1

Introduction

1.1. Nanoindentation

Nanoindentation has been used to probe small-scale mechanical properties, which are relevant to a wide range of materials and applications. During nanoindentation, an indenter tip is brought into contact with a specimen and mechanically loaded with very fine control of load and displacement. As the indenter tip is pressed into the surface of a test material with a prescribed loading and unloading profile, force and displacement are recorded to provide the continuous variation of indentation load down to levels of micro-Newtons, as a function of the indenter penetration depth down to levels of nanometers. This is the load-displacement curve of nanoindentation (often called the P - h curve), such as a schematic of its typical shape is shown in Figure 1.1.

The most common use of nanoindentation is for the measurement of hardness and elastic modulus [1-3], and there has been considerable progress in the measurement of other mechanical parameters as well, including hardening exponents [4-8], creep parameters [9-13], and residual stresses [14-17]. The technique relies on a continuous measurement of depth of

penetration with increasing load and appears to be have first demonstrated by Pethica in 1981 [18]. The present modern treatments probably begin in 1975 by the researchers showing how the area of contact could be measured using the unloading portion of the load-displacement curve [19]. The most commonly used method of analysis is a refinement of Doerner and Nix [1] approach by Oliver and Pharr [2].

However, nanoindentation may be of even greater importance as a technique for more fundamental inquiries in materials physics [20], such as dislocation behaviors [21-39], mechanical instabilities [40-44], phase transformation [36, 45-56] or mechanical twinning [57-59] during a nanoindentation test. In the past two decades, a veritable revolution has occurred in indentation testing, owing to the development of new sensors and actuators that allow instrumented indentations to be routinely performed on submicron scales and high-resolution load-displacement curves. In addition to improvement of nanoindenter, recently-developed capabilities in in situ imaging, exquisite sample machining, acoustic emission detection, and high-temperature testing now allow more detailed investigation on nanoscale phenomena, and offer many opportunities for future scientific inquiry. The variations of global shape of the load-displacement curve may reflect different mechanical properties from one material to the next, but the signals of discrete physical events underneath the indenter tip during nanoindentation are mostly presented as a change of local details in the load-displacement curve, for

example, slope change in loading curve, and so-called “pop-in” or “pop-out” event.

1.1.1 Nanoindentation System

TriboLab[®] 750 Ubi, Hysitron was used for this research. Along with the indenter, the instrument is equipped with optic, piezo controller, SPM imaging system (Figure 1.2). The 1D, normal force only, transducer assembly consists of the force and displacement sensor (Figure 1.3).

1.1.2 Displacement Measurement

The sensor consists of two fixed outer electrodes, which are driven by AC signals 180° out of phase with each other. Since the drive plates are parallel to each other and closely spaced with respect to the lateral dimensions, the electric field potential between the plates varies linearly. Since the signals applied to the drive plates are equal in magnitude but opposite in polarity at any instant, the electric field potential is maximized at the drive plates and minimized at the site centered directly between the drive plates. The input impedance of the synchronous demodulator is significantly larger than the output impedance of the transducer, so the pickup electrode will assume the same potential present at its position between the drive plates. This results in a bipolar output signal equal in magnitude to the drive plate at maximum

deflection, zero at the center position, and varying in a linear manner between maximum displacement and the center position.

1.1.3 Force Measurement

The force is applied to the transducer electrostatically. To apply a force, a large DC bias is applied to the bottom plate of the capacitor. This will create an electrostatic attraction between the center plate and the bottom plate, which will pull the center plate down. The force can be calculated from the magnitude of the voltage applied.

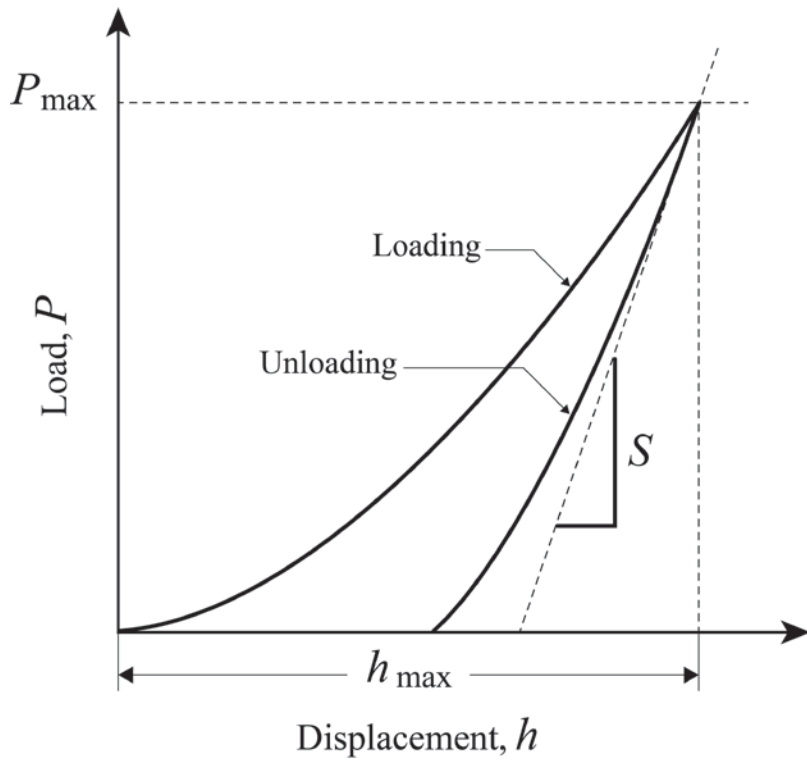


Figure 1.1. Schematic of typical load-displacement curve during loading-unloading cycle where h_{\max} is the maximum indenter displacement at peak indentation load P_{\max} , and S is the contact stiffness (after Oliver and Pharr [2]).



Figure 1.2. The nanoindentation system used in this study, TriboLab[®]
750Ubi, Hysitron

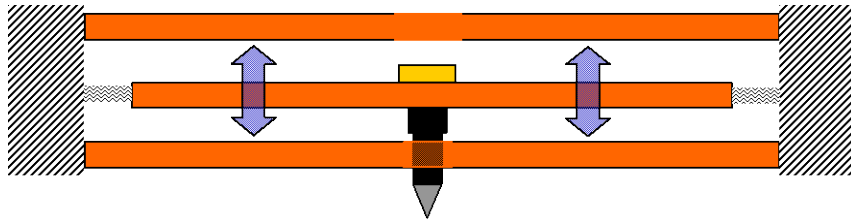


Figure 1.3. Schematic of 1-dimensional transducer.

1.2. Pop-in behavior during nanoindentation

When metallic materials undergo irreversible permanent deformation, discrete physical events, such as dislocation nucleation [21-39], dislocation source activation [34,35], phase transformation [36,45-56] and mechanically induced twinning [57-59] can produce geometrical softening. Once a material experiences geometrical softening during load-controlled indentation, the indenter tip must react rapidly as the softening occurs in order to maintain a constant loading rate in load control. The motion of the tip will be detected as discontinuities on the loading segment of the load-displacement curve, and this sudden displacement excursion is referred to in the literature as a “pop-in”, such as an example shown in Figure 1.4 [30].

Among these, the most popular example of nanoindentation pop-in is the onset of plasticity resulting from dislocation nucleation or dislocation source activation. Gane and Bowden [60] were the first to observe the excursion phenomena on an electropolished surface of gold and also on copper and aluminium surfaces. A fine tip was pressed on the gold surface, but no permanent penetration was observed until some critical load was reached. In metals, the initial indentation behavior corresponds to elastic deformation. However, as the load increases, the material undergoes irreversible plastic deformation at some point, and this onset of plastic behavior generally observed to coincide with a relaxation event in nanoindentation, a pop-in. For

materials with low dislocation densities and step-free surfaces, it is now well established that the first pop-in corresponds to the homogeneous nucleation of dislocations in the highly stressed region beneath the indenter at the theoretical strength. As such, pop-in has become an important tool for measuring the theoretical strength and studying the fundamental mechanisms of dislocation nucleation.

In this case, it is known that the critical load where a pop-in occurs decreases as the surface roughness, dislocation density and the indenter tip radius increases [32-35,61]. Rough surface, high dislocation density, large tip radius increases probability that pre-existing dislocations to move before the applied stress to reach a high value to nucleate a dislocation. In contrast, when they are low or small, probability of homogeneous dislocation nucleation increases which needs much higher stress to occur. This is another type of indentation size effect that is based not on the measured hardness, which depends on the yielding and work-hardening behavior of the material, but rather on the stress needed to initiate dislocation plasticity. Because of this, a flat, smooth and un-strained sample surface is essential and controlling sample surface is very important process in nanoindentation testing, especially when investigating pop-in.

However, geometrical softening behaviors are also able to happen by operation of some other microstructural or crystallographic changes, besides the ordinary elastic to plastic deformation transition case. Many experimental

investigations were reported that pop-in can also be originated from discrete atomic arrangements such as shear band formation in metallic glasses, phase transformations, or mechanical twinning. By itself, nanoindentation often allows the detection of such events under a reasonably well-defined stress state. However, when the technique is augmented by additional testing-measuring methods, near-atomic level details of deformation physics can be deduced. As these techniques become more refined and their synergy with nanoindentation equipment improves, it is expected that the resulting experimental data will play a key role in the development of consistent theories of material behavior at the nanoscale [20].

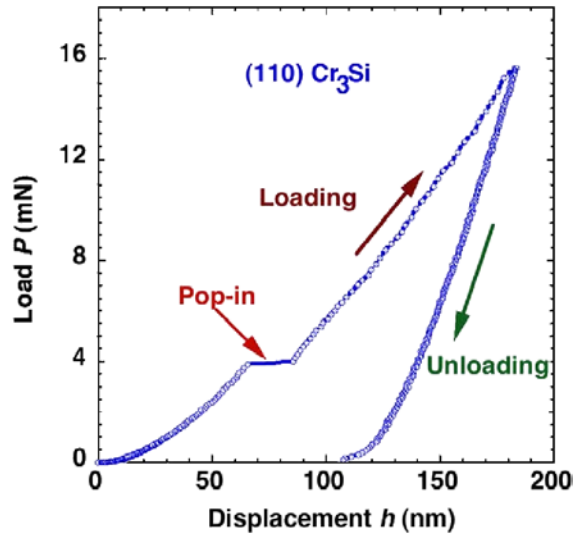


Figure 1.4. Example of “pop-in” event obtained during nanoindentation of an elastic-plastic material, in this case single crystal Cr_3Si (110) [30].

1.3. Hertzian elastic contact theory

In metals, the initial indentation behavior is completely elastic, with fully reversible loading. In general, the elastic deformation region in nanoindentation is often identified by comparing the experimentally obtained load-displacement with the Hertzian elastic contact theory. In the contact between a rigid sphere and a flat surface as shown in Figure 1.5, Hertz found that the contact radius a is related to the applied load P , the indenter radius R , and the elastic properties of the contacting bodies [62-64]. When $R \gg a$, the relationship is given by:

$$a^3 = \frac{3 PR}{4 E_r} \quad (1.1)$$

where E_r is the effective (or reduced) modulus of indentation. For an isotropic elastic material, the effective indentation modulus E_r in Equation 1.1 is related to the elastic moduli of the sample and indenter as follows:

$$\frac{1}{E_r} = \frac{(1-\nu_i^2)}{E_i} + \frac{(1-\nu_s^2)}{E_s} \quad (1.2)$$

where ν and E are the Poisson's ratio and Young's modulus, respectively. The

subscripts i and s refer to the indenter and sample, respectively. If both contacting bodies have a curvature, then R in the above equations is their relative radii given by:

$$\frac{1}{R} = \frac{1}{R_1} + \frac{1}{R_2} \quad (1-3)$$

In Equation 1.3 we set the radius of the indenter to be positive always, and the radius of the specimen to be positive if its center of curvature is on the opposite side of the lines of contact between the two bodies.

It is important to realize that the deformations at the contact are localized and the Hertz equations are concerned with these and not the bulk deformations and stresses associated with the method of support of the contacting bodies. The deflection h of original free surface in the vicinity of the indenter is given by:

$$h = \frac{1}{E_r} \frac{3}{2} \frac{P}{4a} \left(2 - \frac{r^2}{a^2} \right) \quad r \leq a \quad (1.4)$$

where r is the distance from the indenting center at the surface.

It can be easily shown from Equation 1.4 that the depth of the circle of contact beneath the specimen free surface is half of the total elastic

displacement. That is, the distance from the specimen free surface to the depth of the radius of the circle of contact at full load is $h_a=h_p=h_{\max}/2$:

The distance of mutual approach of distant points in the indenter and specimen is calculated from:

$$\delta^3 = \left(\frac{3}{4E_r} \right)^2 \frac{P^2}{R} \quad (1.5)$$

Substituting Equation 1.4 into Equation 1.1, we can express the distance of mutual approach as:

$$\delta = \frac{a^2}{R} \quad (1.6)$$

For the case of a non-rigid indenter, if the specimen is assigned a modulus of E_r , then the contact can be viewed as taking place between a rigid indenter of radius R . δ in Equation 1.5 becomes the total depth of penetration h_{\max} beneath the specimen free surface. Rearranging Equation 1.5 slightly, the classical relationship between elastic displacement of penetration by a sphere h and the applied load P is obtained:

$$P = \frac{4}{3} E_r R^{1/2} h_{\max}^{3/2} \quad (1.7)$$

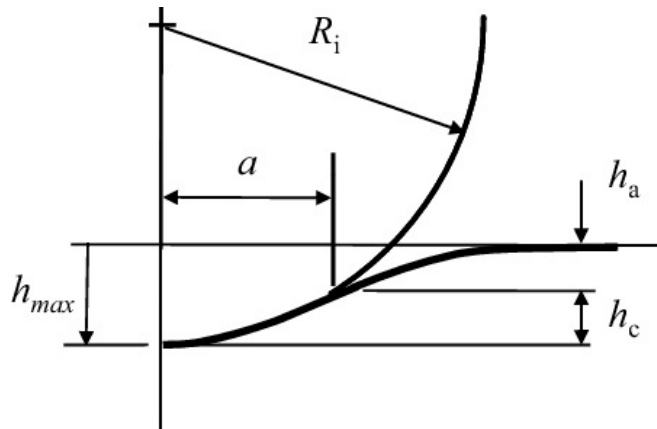


Figure 1.5. Schematic of contact between a rigid indenter and a flat specimen with modulus E . The radius of the circle of contact is a , and the total depth of penetration is h_{max} . h_a is the depth of the circle of contact from the specimen free surface, and h_c is the distance from the bottom of the contact to the contact circle (the contact depth).

1.4. Thesis motivations

The response of a material to nanoindentation is usually presented in the form of a load–displacement curve and variety of information can be obtained from the curve. Among them, investigation on a pop-in observed in the load-displacement curves has mainly been focused on describing it as the elastic-to-plastic deformation transition of metallic materials, based on a Hertzian analysis of the elastic portion of the load–displacement curve. However, as introduced in previous sections, the source of pop-in is basically geometrical softening behaviors, which means that some other microstructural or crystallographic changes excluding the case of the incipient plasticity can be the origin of geometrical softening as well.

In this study, experimental evidences of close relationship between pop-in and several physical events during nanoindentation of steel were investigated. Three different types of steel were used to examine mechanically induced martensitic transformation (α') and epsilon martensite formation (ϵ) from austenite, and breaking and recovery of Cottrell atmosphere in ferrite during nanoindentation, respectively.

In order to perform nanoindentation exactly on the position of interest and to examine closely the situation underneath the indenter tip, variety of testing and measuring instruments, such as electron backscattered diffraction (EBSD), scanning probe microscopy (SPM), nanoindentation, focused ion

beam (FIB) and high-resolution transmission electron microscopy (HR-TEM), were used. Together with developing a combination method of testing-measuring machines, a special surface treatment method for nanoindentation of multiphase steels which have multiple phases with very different etching and polishing characteristics was also developed to obtain a flat, smooth and un-damaged specimen surface.

1.5. References

- [1] M.F. Doerner, W.D. Nix : *J. Mater. Res.*, 1986, vol. 1, pp. 601-609.
- [2] W.C. Oliver, G.M. Pharr : *J. Mater. Res.*, 1992, vol. 7, pp. 1564-1583.
- [3] W.C. Oliver, G.M. Pharr : *J. Mater. Res.*, 2004, vol. 19, pp. 3-20.
- [4] M. Dao, N. Chollacoop, K.J. Van Vliet, T.A. Venkatesh, S. Suresh : *Acta Mater.*, 2001, vol. 49, pp. 3899-3918.
- [5] N. Chollacoop, M. Dao, S. Suresh : *Acta Mater.*, 2003, vol. 51, pp. 3713-3729.
- [6] J.L. Bucaille, S. Stauss, E. Felder, J. Michler : *Acta Mater.*, 2003, vol. 51, pp. 1663-1678.
- [7] S. Kucharski, Z. Mróz : *Mater. Sci. Eng. A*, 2001, vol. 318, pp. 65-76.
- [8] D. Ma, C.W. Ong, J. Lu, J. He : *J. Appl. Phys.*, 2003, vol. 94, pp. 288-294.
- [9] A.C. Fischer-Cripps : *Mater. Sci. Eng. A*, 2004, vol. 385, pp. 74-82.
- [10] M.L. Oyen, R.F. Cook : *J. Mater. Res.*, 2003, vol. 18, pp. 139-150.
- [11] B. Storåkers, P.-L. Larsson : *J. Mech. Phys. Solids*, 1994, vol. 42, pp. 307-332.
- [12] B.N. Lucas, W.C. Oliver : *Metall. Mater. Trans. A*, 1999, vol. 30, pp. 601-610.
- [13] H. Takagi, M. Dao, M. Fujiwara, M. Otsuka : *Philos. Mag.*, 2003, vol. 83, pp. 3959-3976.

- [14] S. Suresh, A.E. Giannakopoulos : *Acta Mater.*, 1998, vol. 46, pp. 5755-5767.
- [15] S. Carlsson, P.-L. Larsson : *Acta Mater.*, 2001, vol. 49, pp. 2179-2191.
- [16] S. Carlsson, P.-L. Larsson : *Acta Mater.*, 2001, vol. 49, pp. 2193-2203.
- [17] J.G. Swadener, B. Taljat, G.M. Pharr : *J. Mater. Res.*, 2001, vol. 16, pp. 2091-2102.
- [18] J.B. Pethica : *Third International Conference on Modification of Surface Properties of Metals by Ion-implantation*, Manchester, England, 23-26, 1981, V. Ashworth et al. eds., Pergamon Press, Oxford, 1982, pp. 147-157S.
- [19] S.I. Bulychev, V.P. Alekhin, M.Kh. Shorshorov, A.P. Ternorskii : *Zavod. Lab.*, 1975, vol. 41, pp. 1137-1140.
- [20] C.A. Schuh : *Materials Today*, 2006, vol. 9, pp. 32-40.
- [21] W.W. Gerberich, J.C. Nelson, E.T. Lilleodden, P. Anderson, J.T. Wyrobek : *Acta Mater.*, 1996, vol. 44, pp. 3585-3598.
- [22] S.G. Corcoran, R.J. Colton, E.T. Lilleodden, W.W. Gerberich : *Phys. Rev. B.*, 1997, vol. 55, pp. R16057-R16060.
- [23] D.F. Bahr, D.E. Kramer, W.W. Gerberich : *Acta Mater.*, 1998, vol. 46, pp. 3605-3617.
- [24] C.L. Kelchner, S.J. Plimpton, J.C. Hamilton : *Phys. Rev. B*, 1998, vol. 58, pp. 11085-11088.
- [25] E.B. Tadmor, R. Miller, R. Phillips, M. Ortiz : *J. Mater. Res.*, 1999, vol.

- 14, pp. 2233-2250.
- [26] A. Gouldstone, H.-J. Koh, K.-Y. Zeng, A.E. Giannakopoulos, S. Suresh : *Acta Mater.*, 2000, vol. 48, pp. 2277-2295.
- [27] M. Göken, M. Kempf : *Z. Metallkd.*, 2001, vol. 92, pp. 1061-1067.
- [28] A. Gouldstone, K.J. Van Vliet, S. Suresh : *Nature*, 2011, vol. 411, pp. 656.
- [29] E.T. Lilleodden, J.A. Zimmerman, S.M. Foiles, W.D. Nix : *J. Mech. Phys. Solids*, 2003, vol. 51, pp. 901-920.
- [30] H. Bei, E.P. George, J.L. Hay, G.M. Pharr : *Phys. Rev. Lett.*, 2005, vol. 95, 045501.
- [31] T. Ohmura, K. Tsuzaki : *J. Mater. Sci.*, 2007, vol. 42, pp. 1728-1732.
- [32] A.A. Zbib, D.F. Bahr : *Metall. Mater. Trans. A.*, 2007, vol. 38, pp. 2249-2255.
- [33] H. Bei, Y.F. Gao, S. Shim, E.P. George, G.M. Pharr : *Phys. Rev. B*, 2008, vol. 77, 060103(R).
- [34] S. Shim, H. Bei, E.P. George, G.M. Pharr : *Scripta Mater.*, 2008, vol. 59, pp. 1095-1098.
- [35] A. Barnoush, M.T. Welsch, H. Vehoff : *Scripta Mater.*, 2010, vol. 63, pp. 465-468.
- [36] T.-H. Ahn, C.-S. Oh, D.H. Kim, K.H. Oh, H. Bei, E.P. George, H.N. Han : *Scripta Mater.*, 2010, vol. 63, pp. 540-543.
- [37] S.M. Han, T. Bozorg-Grayeli, J.R. Groves, W.D. Nix : *Scripta Mater.*,

- 2010, vol. 63, pp. 1153-1156.
- [38] C. Begau, A. Hartmaier, E.P. George, G.M. Pharr : *Acta Mater.*, 2011, vol. 59, pp. 934-942.
- [39] T.-H. Ahn, C.-S. Oh, K. Lee, E.P. George, H.N. Han : *J. Mater. Res.*, 2011, vol. 27, pp. 39-44.
- [40] J.G. Wang, B.W. Choi, T.G. Nieh, C.T. Liu : *J. Mater. Res.*, 2000, vol. 15, pp. 798-807.
- [41] Yu.I. Golovin, V.I. Ivolgin, V.A. Khonik, K. Kitagawa, A.I. Tyurin : *Scripta Mater.*, 2001, vol. 45, pp. 947-952.
- [42] C.A. Schuh, T.G. Nieh, Y. Kawamura : *J. Mater. Res.*, 2002, vol. 17, pp. 1651-1654.
- [43] C.A. Schuh, T.G. Nieh : *J. Mater. Res.*, 2004, vol. 19, pp. 46-57.
- [44] B. Moser, J. Kübler, H. Meinhard, W. Muster, J. Michler : *Adv. Eng. Mater.*, 2005, vol. 7, pp. 388-392.
- [45] G.M. Pharr, W.C. Oliver, D.R. Clarke : *Scripta Metall.*, 1989, vol. 23, pp. 1949-1952.
- [46] G.M. Pharr, W.C. Oliver, D.S. Harding : *J. Mater. Res.*, 1991, vol. 6, pp. 1129-1130.
- [47] T.F. Page, W.C. Oliver, C.J. McHargue : *J. Mater. Res.*, 1992, vol. 7, pp. 450-473.
- [48] D.L. Callahan, J.C. Morris : *J. Mater. Res.*, 1992, vo. 7, pp. 1614-1617.
- [49] E.R. Weppelmann, J.S. Field, M.V. Swain : *J. Mater. Res.*, 1993, vol. 8,

- pp. 830-840.
- [50] E.R. Weppelmann, J.S. Field, M.V. Swain : *J. Mater. Sci.*, 1995, vol. 30, pp. 2455-2462.
- [51] H.N. Han, D.-W. Suh : *Acta Mater.*, 2003, vol. 51, pp. 4907-4917.
- [52] H.N. Han, C.G. Lee, C.-S. Oh, T.-H. Lee, S.-J. Kim : *Acta Mater.*, 2004, vol. 52, pp. 5203-5214.
- [53] J.-I. Jang, M.J. Lance, S. Wen, T.Y. Tsui, G.M. Pharr : *Acta Mater.*, 2005, vol. 53, pp. 1759-1770.
- [54] H.N. Han, C.-G. Lee, D.-W. Suh, S.-J. Kim : *Mater. Sci. Eng. A.*, 2008, vol. 485, pp. 224-233.
- [55] H.N. Han, C.-S. Oh, G. Kim, O. Kwon : *Mater. Sci. Eng. A.*, 2009, vol. 499, pp. 462-468.
- [56] M.-G. Lee, S.-J. Kim, H.N. Han : *Int. J. Plas.*, 2010, vol. 26, pp. 688-710.
- [57] J.E. Bradby, J.S. Williams, J. Wong-Leung, M.V. Swain, P. Munroe : *Appl. Phys. Lett.*, 2002, vol. 80, pp. 2651-2653.
- [58] R.D.K. Misra, Z. Zhang, Z. Jia, M.C. Somani, L.P. Karjalainen : *Scripta Mater.*, 2010, vol. 63, pp. 1057-1060.
- [59] R.D.K. Misra, Z. Zhang, Z. Jia, P.K.C. Venkat Surya, M.C. Somani, L.P. Karjalainen : *Mater. Sci. Eng. A*, 2011, vol. 528, pp. 6958-6963.
- [60] N. Gane, F.P. Bowden : *J. Appl. Phys.*, 1968, vol. 39, pp. 1432-1435.
- [61] Y. Shibutani, A. Koyama : *J. Mater. Res.*, 2004, vol. 19, pp. 183-188.

- [62] H. Hertz : J. Reine Angew. Math., 1881, vol. 92, pp. 156-171.
Translated and reprinted in English in *Hertz's Miscellaneous Papers*,
Macmillan & Co., London, England, 1986, Ch. 5.
- [63] K.L. Johnson : *Contact Mechanics*, Cambridge Univ. Press, Cambridge,
England, 1985, pp. 84-106.
- [64] A.C. Fischer-Cripps : *Nanoindentation*, Springer-Verlag New York,
Inc., New York, USA, 2002, pp. 1-3.

Chapter 2

Investigation of strain-induced martensitic transformation ($\gamma \rightarrow \alpha'$) in metastable austenite

2.1. Introduction

In recent years, steels that undergo transformation-induced plasticity, the so-called TRIP steels, have attracted considerable interest in the automotive industry on account of their remarkable balance of high strength and good ductility, as shown in Figure 2.1. This aspect of TRIP steels basically originates from a solid state phase transformation of metastable FCC austenite into BCT martensite during deformation [1-3]. The replacement of austenite by the much harder martensite increases the strain hardening rate and effectively delays the onset of local necking during straining. In addition, the transformation-induced strain contributes to improved ductility [4-6]. Therefore, the stability of the metastable austenite phase is the most important factor in the alloy design and processing of multiphase TRIP steels [3, 7]. However, there are few reports on the mechanical behavior and stability of the individual austenite grains in multiphase TRIP steels [8] due to the difficulty of making such small-scale measurements.

This chapter reports experimental results of nanoindentation and

microstructural studies to provide micromechanical insight into the strain-induced phase transformation and deformation behavior of metastable austenite in TRIP steel. Sequential experiments were carried out, first using electron backscattered diffraction (EBSD) to map the phase and orientation distributions of the grains, followed by nanoindentation of individual austenite grains in the mapped region, then sectioning through an indent using focused ion beam (FIB) milling and finally transmission electron microscopy (TEM) to confirm the formation of martensite from austenite under the indent. In addition, the load-displacement curves of the metastable austenite phase were analyzed to identify signatures of the strain-induced martensitic transformation.

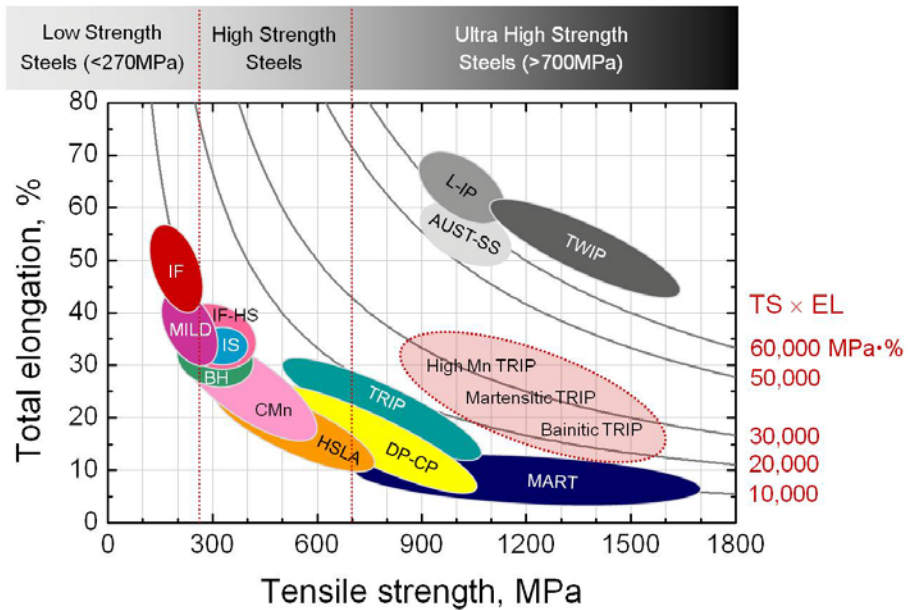


Figure 2.1. A graphical plot (often called “a banana curve”) that shows change in total elongation as a function of yield strength for various steel products. The strength-ductility balance (tensile strength \times elongation) is often used as an index for mechanical characteristics or efficiency of steel products.

2.2. Experimental procedures

2.2.1. Sample preparation

For the convenience of nanoindentation of each austenite grain, the composition of the TRIP steel used in this study was designed as Fe-0.08C-0.5Si-1Al-7Mn (wt.%) to get much higher fraction of austenite phase compared to conventional TRIP steels [9]. Since it was received in the cold-rolled state, it was first heated to 915K and held for 24 hours to induce reverse transformation of the rolling induced martensite into austenite and then air cooled to room temperature. A schematic diagram for heat treatment process and the microstructure change during the process are shown in Figure 2.2 and Figure 2.3, respectively.

EBSD was used for phase identification on the flat surface of the TRIP steel. Since a TRIP-aided multiphase steel consists of multiple phases with very different etching and polishing characteristics, and moreover, the metastable austenite can easily be transformed to martensite during mechanical polishing, a special surface treatment method for both EBSD and nanoindentation is essential to obtain a flat, smooth and un-damaged specimen surface. In this study, the specimen was prepared by repeated electro-polishing with a 10% perchloric acid-90% ethyl alcohol solution, etching with a 4% HF-96% hydrogen peroxide solution and gentle polishing with SiC paper to remove the mechanically damaged layer. Details for surface

control will be introduced later in the section 2.4. Figure 2.4 shows an SEM image and the corresponding EBSD phase map of the TRIP steel samples, showing well-defined FCC austenite and BCC ferrite grains with a mean grain size of approximately 0.7 μm . The volume fraction of austenite and ferrite was measured 28.6 % and 59.7 %, respectively. The rest of unindexed 11.7 % corresponds to grain boundaries, which was extrapolated and enhanced to the nearest grains in Figure 2.4(b).

2.2.2. Measuring procedure

After obtaining phases and locations of grains in the interested area by EBSD, nanoindentation tests were performed using a Hysitron TriboLab 750 Ubi nanoindentation system in load control at a constant loading rate of 200 $\mu\text{N/s}$ up to a maximum load of 1000 μN . A Berkovich type indenter with a centerline-to-face angle of 65.3° was used. A scanning probe microscope (SPM) was available in the system which made it possible to evaluate grain morphologies and identify precisely those areas that had been previously analyzed by EBSD. Figure 2.5(a) shows a magnified image of the square-marked area in Figure 2.4(b) and Figure 2.5(c) is an SPM image of the specimen surface after nanoindentation where the circled area is the same as that circled in Figure 2.5(a). Guided by the EBSD and SPM images, individual austenite grains were selected for nanoindentation after which the

indented areas were analyzed again by scanning electron microscopy (SEM) and EBSD to determine if the indents lay entirely within single austenite grains. Cross section TEM analysis of the indented specimen was performed to check for strain-induced martensite in the region directly under the indent. The TEM sample was prepared by focused ion beam (FIB) milling along the dotted lines marked in Figure 2.5(d). The overall procedure of sequential experiments is described well in Figure 2.6.

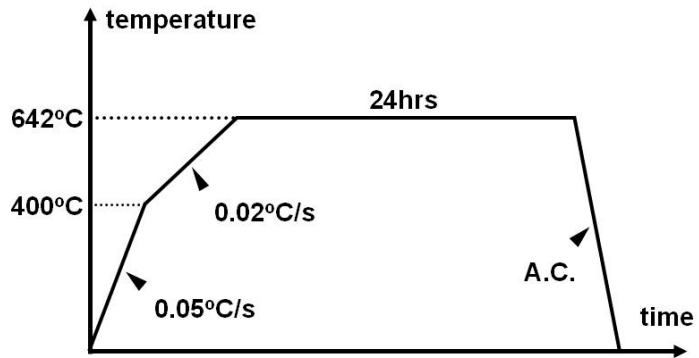


Figure 2.2. Temperature history of the steel for reverse transformation. The specimens were batch annealed.

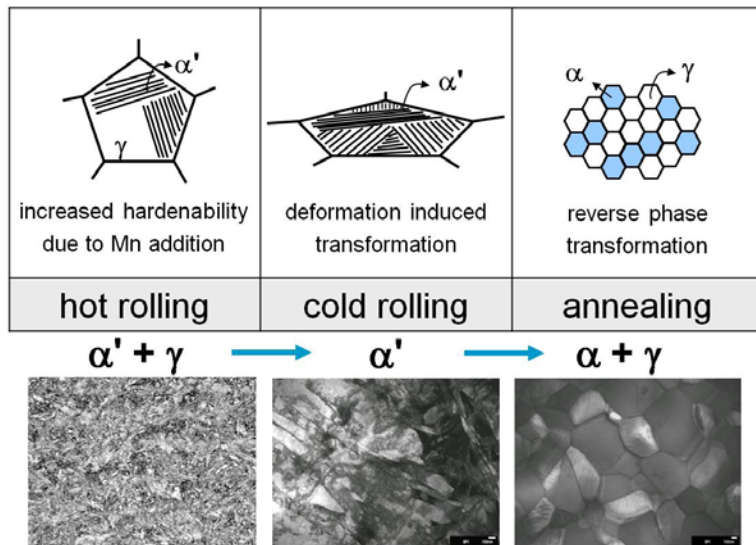
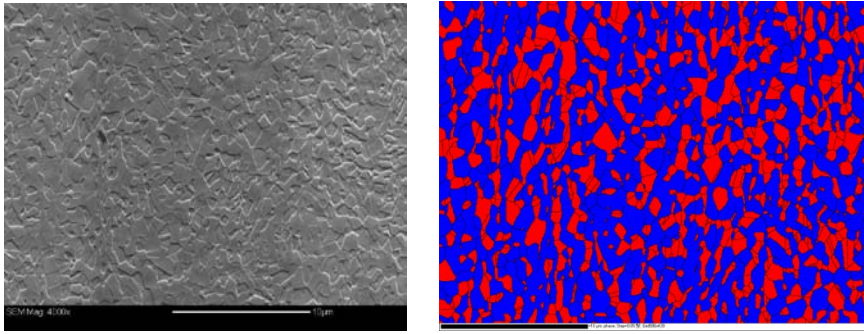


Figure 2.3. Microstructure change upon reverse transformation.



(a)

(b)

Figure 2.4. Microstructure of the sample. (a) SEM image, (b) EBSD phase map. Red grains are FCC austenite and blue are BCC ferrite.

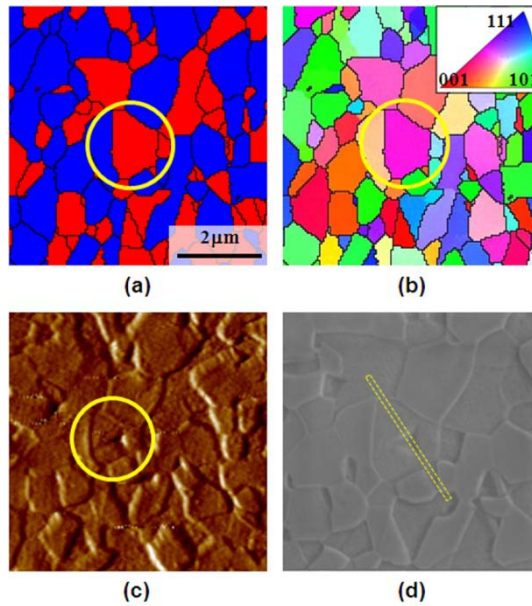


Figure 2.5. (a) EBSD phase map (Red: FCC, Blue: BCC), (b) orientation map of sample surface before indentation, (c) SPM image of indent in metastable austenite grain (yellow circle) and (d) Dotted yellow lines on SEM image showing schematically where FIB milling was used to cut out a cross-section through the indent for TEM analysis.

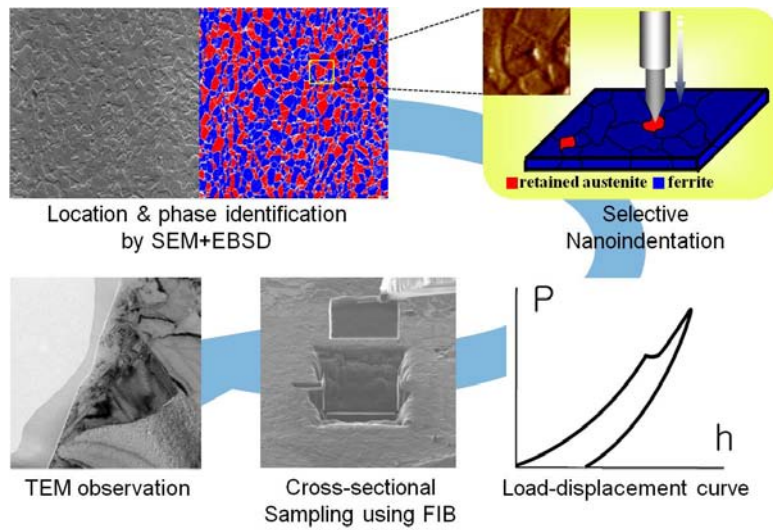


Figure 2.6. Sequential experiment procedures for measuring martensitic transformation from metastable austenite.

2.3. Results and discussion

Figure 2.7 gives the load-displacement curve (black symbols) obtained by nanoindentation of the circled metastable austenite grain in Figure 2.5. Three pop-ins are present on the otherwise smooth loading segment of this load-displacement curve. Similar pop-ins were observed for most of the austenite grains indented in this study. On carefully polished metal surfaces the deformation before the first pop-in has been shown to be perfectly elastic (e.g. [10,11]). Assuming that the indenter tip is spherical at shallow depths, the experimental data before the first pop-in can be compared with the Hertzian elastic contact solution [12]:

$$P = \frac{4}{3} E_r \sqrt{R h^3}, \quad (2.1)$$

where P is the load applied, h is the corresponding indentation depth, R is the radius of the indenter tip, and E_r is the effective (or reduced) modulus of indentation. The radius of our indenter tip was determined to be 200nm from a calibration using standard fused quartz. According to Gouldstone et al. [13], for an indenter tip radius of 200nm and centerline-to-face angle of 65.3°, the depth at which the tip geometry transitions from spherical to Berkovich is approximately 36.5nm. Figures 2.8(a) and (b) show a typical Berkovich tip

and a schematic of the idealization of the indenter tip as a sphere, respectively. Therefore, we assume here that at depths below about 20nm in Figure 2.7, where the first pop-in occurs, indentation occurs with a spherical tip.

For an isotropic elastic material, the effective indentation modulus E_r in Equation (2.1) is related to the elastic moduli of the sample and indenter as follows:

$$\frac{1}{E_r} = \frac{1-\nu_i^2}{E_i^2} + \frac{1-\nu_s^2}{E_s^2}, \quad (2.2)$$

where ν and E are the Poisson's ratio and Young's modulus, respectively. The subscripts i and s refer to the indenter and sample, respectively. For an anisotropic material, a similar expression can be written if the isotropic moduli E_r and E_s are replaced with M_r and M_s , the so-called indentation moduli [14,15]. In general, the indentation modulus (M_s) is a complicated function of the single crystal elastic constants. However, for cubic crystals, Vlassak and Nix [14,15] have shown that M_s for a given (hkl) plane can be obtained from the isotropic E_s and ν_s by multiplying with a correction factor β_{hkl} for that plane, i.e.,

$$M_{hkl} = \beta_{hkl} \left(\frac{E_s}{1 - \nu_s^2} \right). \quad (2.3)$$

Additionally, the correction factor can be expressed as:

$$\beta_{hkl} = a + c(A - A_0)^B \quad (2.4)$$

where the constants a , c , A_0 and B are functions of Poisson's ratio $\nu_{\langle 001 \rangle}$ and A the shear anisotropy factor. Here, $\nu_{\langle 001 \rangle}$ was determined to be 0.337 from the relationship [16] between the components of elastic compliance, which was computed from an atomistic simulation [17]. Next, the following parameter values were determined $a = 1.243$, $c = -0.243$, $B = 0.296$ and $A_0 = 0$ from the data provided by Vlassak and Nix [15] for the (001) surface which we assume here is close enough in orientation to the (113) austenite grain shown in Figure 2.5(b). Finally, using a value of $A = 1.756$ for steel [17], $\beta_{hkl} = 0.956$ was obtained. By combining the isotropic elastic constants ($E_s = 199$ GPa and $\nu_s = 0.29$ [17]) and the correction factor β_{hkl} , the effective anisotropic indentation modulus, M_r , was calculated from Equations 2.2 and 2.3.

The theoretical (Hertzian) elastic behavior during indentation was calculated using this effective modulus of austenite at room temperature and the isotropic elastic constants of the diamond tip, $E_i = 1141$ GPa and $\nu_i = 0.07$

[11], and the results are shown by the blue dashed line in Figure 2.7. Before the first pop-in, the theoretical curve matches the experimental loading curve well indicating that the region below the first pop-in is elastic while that above it is plastic. In the elastic regime, Hertzian analysis [12] gives the maximum shear stress underneath the indenter, τ_m , as follows:

$$\tau_m = 0.31 \left(\frac{6PE_r^2}{\pi^3 R^2} \right)^{1/3} . \quad (2.5)$$

Using the above equation and the first pop-in load, τ_m was determined to be 9.4 GPa. Since the shear modulus G of austenite at room temperature is 76.8 GPa [17], the above value of τ_m is approximately $G/8$, which is within the range of values for the theoretical yield strength of a crystalline material [18]. This result is consistent with the very small and well-annealed austenite grains in our specimen. According to Shim et al. [11], low dislocation density and small tip radius increases probability that pre-existing dislocations to move before the applied stress to reach a high value to nucleate a dislocation. In contrast, probability of homogeneous dislocation nucleation which needs much higher stress than pre-existing dislocation moving increases as dislocation density and/or the indenter tip radius decreases. A schematic diagram shown in Figure 2.9 [11] describes well this indentation size effect

that is based on the stress needed to initiate dislocation plasticity. The dislocation density in well-annealed metals is about 10^{10} m^{-2} [19], which gives a mean distance between dislocations of about 10 μm . Since the size of the indented austenite grain is much smaller, about 1.2 μm , the region in the high-stress zone underneath the indenter is likely to be free of mobile dislocations at least for small penetration depths of around 20 nm, where the first pop-ins occur. Therefore, the first pop-in event is likely the result of dislocation nucleation [11, 13, 20-25].

After the first pop-in, there are two more pop-ins that begin at depths of ~ 25 and 50 nm, as shown in Figure 2.7. It is possible that these are related to the formation of strain-induced martensite in the metastable austenite. To check for the presence of martensite in the indented region, the cross-section of a sample indented to a depth of ~ 70 nm, which is slightly beyond the third pop-in, was examined by TEM. As shown in the bright field TEM image in Figure 2.10(a), there is an obvious indent on the surface and two regions with distinctly different morphologies inside the grain adjacent to the indent. From an analysis of the diffraction patterns for these two regions (Figures 2.10(b) and (c)), the region closest to the indent was determined to be transformed martensite while the rest of the parent grain remained as austenite with some stacking faults. This microstructural observation strongly suggests that one of the pop-ins on the load-displacement curve corresponds to the onset of a

strain-induced martensitic transformation. Additional, higher-resolution experiments are needed to better correlate a single pop-in with the observed phase transformation.

In connection with the above observations, an interesting question is why the formation of strain-induced martensite causes a pop-in during nanoindentation. A second related question is whether the magnitude of the pop-in can be rationalized in terms of the transformation strain. Since martensite is much harder than austenite, and the lattice parameter of martensite is larger than that of austenite, the appearance of martensite during deformation must increase the strain hardening rate. Therefore, the softening implied by the pop-ins must be explained. In this study, an attempt is made to understand the pop-in behavior using the concept of favorable variant selection in the strain-induced martensite during nanoindentation.

It is well known that transformed martensite usually has an orientation relationship with its parent austenite phase, referred to as the Kurdjumov–Sachs (K–S) relation [26]. Because of the cubic symmetry, there are 24 equivalent variants in K-S relationship, as listed in Table 2.1. Each of the 24 K-S variants has one compressive axis and two tensile axes for the martensitic transformation, as shown in Figure 2.11, which is called the Bain distortion. The mechanical interaction energy, U_i , for the i th martensitic variant is a function of the applied stress, σ_{ij} and the lattice strain in austenite during the phase transformation [5]:

$$U^i = m_v \sigma_{ij} \cdot \varepsilon_{ij}^i \quad (2.6)$$

where ε_{ij}^i is the transformation strain for the i th martensite variant in the specimen coordinate system, which can be calculated by the tensor transformation rule linking the crystal coordinate system to the specimen coordinate system, and m_v is the molar volume of austenite. The differences in the mechanical interaction energies of the different variants causes the selection of a specific martensite variant that minimizes the total energy, which is required during the strain-induced phase transformation of metastable austenite [5, 27, 28]. In the nanoindentation of a single austenite grain, the dominant external stress was assumed to be the compressive stress along the surface normal direction of the sample, although the stress state underneath the indenter is complex, as an FEM simulation result for spherical indenter in Figure 2.12. Therefore, it is natural that a variant whose compressive axis of the Bain distortion is nearly parallel to the indentation direction should have a higher probability of selection. Moreover, since the martensitic transformation is a nucleation-controlled process and its speed is quite fast, the indenter tip must react rapidly as the strain-induced phase transformation occurs in order to maintain a constant loading rate in load control, which leads to a pop-in.

If the pop-ins during plastic deformation were originated from strain-induced martensitic transformation, the magnitude of these pop-ins should correspond to the transformation-induced plastic (TRIP) strain and the load at the pop-in should be closely related to the stability of the individual austenite grain. In this study, a simple calculation for the TRIP strain was made by considering crystal geometry change under the indenter. An assumption was made that the TRIP strain is introduced only by the Bain deformation. Figure 2.13 shows a schematic of crystal orientation and geometry with a cross-section TEM image underneath the indentation, and also the notations for the terms used in the calculation. In the present austenite grain, the direction of indentation, which should be the normal of bulk sample surface, was measured [113]. If the contraction axis of Bain deformation was chosen to be the most parallel one to the indentation axis it should be [001] of the crystal. The amount of contraction along the indentation direction in a unit cell, d_{unit} , can be expressed as:

$$d_{unit} = (a_{\gamma} - c_{\alpha'}) \cos \theta \quad (2.7)$$

where a_{γ} is the lattice parameter of austenite, $c_{\alpha'}$ is the c-parameter of martensite, and θ is the angle between [113] and [001], respectively. The number of austenite unit cells along the indentation axis is as follows:

$$\text{Number of } \gamma \text{ unit cells} = \frac{L_{\alpha'}}{a_{\gamma} \cos \theta} \quad (2.8)$$

where $L_{\alpha'}$ is the thickness of martensite along the centerline of the indenter tip, as described in Figure 2.13. Then finally, the total amount of contraction along the indentation direction can be predicted by multiplying Equations 2.7 and 2.8, or alternatively, by multiplying the contraction rate, $(a_{\gamma}-c_{\alpha'})/a_{\gamma}$, to the thickness of martensite, $L_{\alpha'}$. In the present case, the total amount of contraction by martensitic transformation was calculated 25.2 nm, which is in good agreement with the measured total amount of pop-in of approximately 20 nm, from the load-displacement data. This calculation result also supports that the pop-ins during plastic deformation were originated from the indentation-induced martensitic transformation.

A less stable austenite in another TRIP steel with different chemical composition was additionally examined. Figure 2.14 shows the load-displacement curve of austenite that circled in the phase map (the inlet), there are more pop-ins measured on the curve than on that of the austenite previously investigated (Figure 2.7). The cross-section TEM studies were also conducted, but in this time, the indented grain in a cross-section plane was automatically examined using an automatic phase and orientation mapping system (ASTAR, NanoMEGAS) equipped in TEM (JEM 2100F, JEOL), with

step size of 20nm. Figures 2.15 (a-c) show a plan-view image, an automatically indexed phase map and an orientation map of region underneath the indent, respectively. As can be seen in Figure 2.15(b), the most part of the grain had transformed to α' martensite (skyblue colored), while the rest of the grain still remained as austenite (peach colored). However, there are many of grain boundaries measured in the transformed martensite region, indicating that the area is not a single martensite grain even though it was one austenite grain before indentation. An orientation map in Figure 2.15(c) shows the multiple martensite more clearly, nine pieces with different orientation are seen in the figure. A remarkable result is that all the nine different martensite packets have K-S orientation relationship with their common parent austenite. The variants for the K-S relation were different for each packet, but they were in the K-S relationship with the misfit angles to the ideal orientations were $\sim 5^\circ$, as shown in Table 2.2.

By applying the stress condition at each martensite positions, which were calculated by crystal plasticity finite element method (CP-FEM) (Figure 2.16), the energetically most favorable variants for each martensite could be predicted based on Wechsler-Lieberman-Reed (W-L-R) crystallographic theory [5,42]. The probability, which a nucleation site would really act, was derived for each variant as a function of the interaction energy between externally applied stress state and lattice deformation (Equation 2.6). As shown in Table 2.2, only 4 martensite packets were in the same variant with those

expected, including the closest one to the indenter. Although the real details might be far more sophisticated, it seems that each martensite packet transformed independently and in sequence. A certain area on which a sufficient stress was applied may have transformed to martensite first. Although the speed of martensitic transformation is quite fast, extension of the transformation process may be stopped by some defects which exist in the grain. At this stage, the stress conditions were changed because austenite grain boundaries can act as barriers, and transformed martensite, much harder than austenite, can act as another indenter. Therefore, the next martensite packets will transform under totally different stress states. The result is multiple martensite packets with different orientations, but all of them are in K-S relation. This situation under the indenter could be reflected on the load-displacement curve as well, resulting in multiple pop-ins.

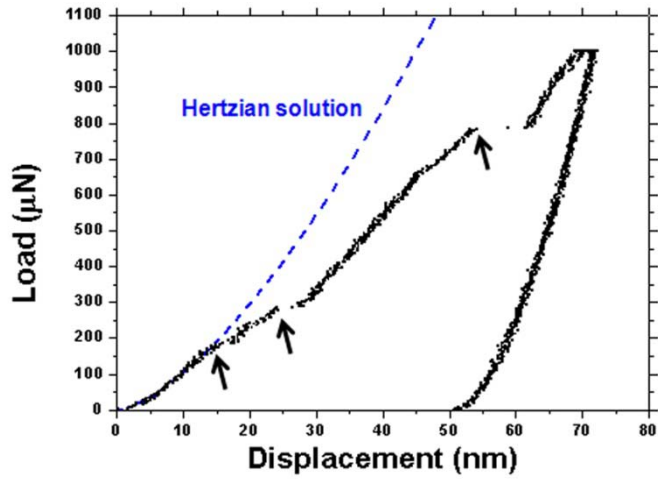
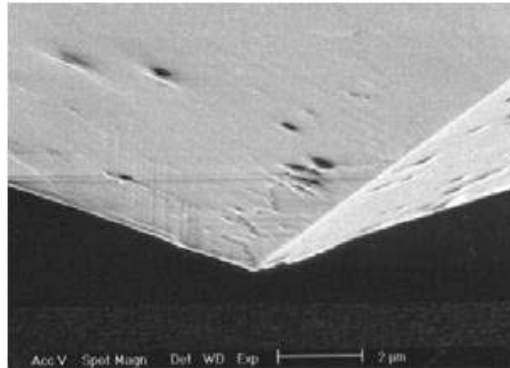
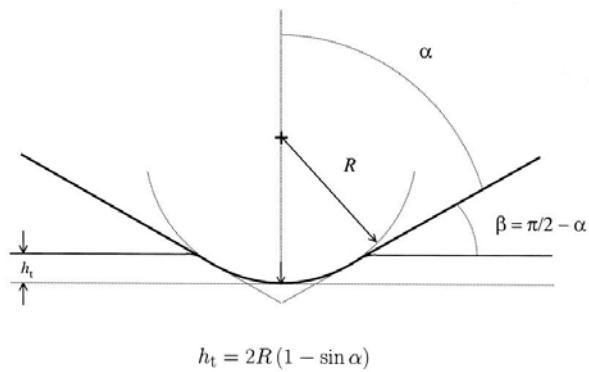


Figure 2.7. Comparison of experimental measurements (black symbols) to prediction of the Hertzian elastic load-displacement behavior (blue dashed line) of the metastable austenite grain shown in Figure 2.5. Arrows indicate the starting points of the three pop-ins.



(a)



(b)

Figure 2.8. (a) A typical image of Berkovich indenter. (b) A schematic of the idealization of the indenter tip as a sphere [13].

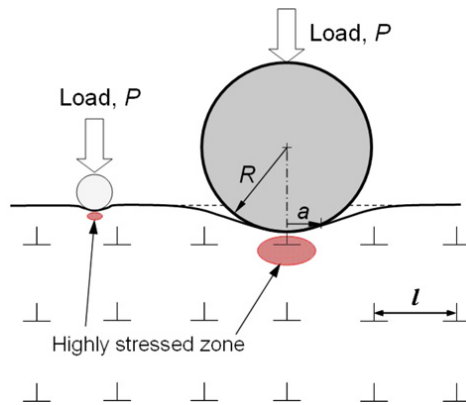


Figure 2.9. Schematic diagram showing the geometry of the nanoindentation test with spherical indenters. Dislocations are idealized as a two dimensional square array with a spacing l [11].

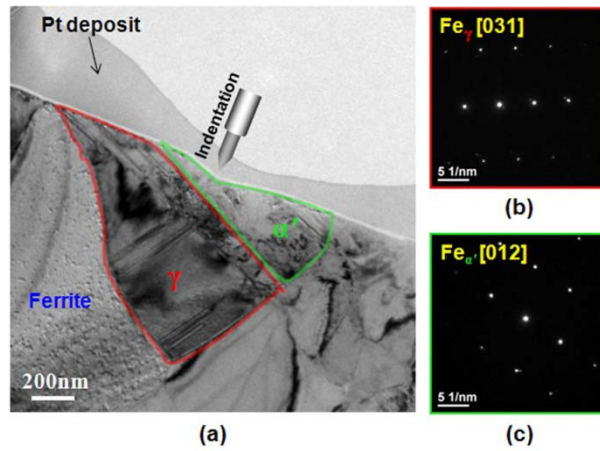


Figure 2.10. (a) Bright field TEM image of the cross-section of a sample indented to a depth slightly beyond the third pop-in of Figure 2. Diffraction patterns from (b) region closest to the ferrite grain in (a) showing that it remains as austenite, γ and (c) region closest to the indenter in (a) showing that it has transformed to martensite, α' .

Table 2.1. The 24 variants of K-S relation.

Variant no.	Plane parallel (γ) // (α')	Direction [γ] // [α']
1	(111) // (011)	[-110] // [-1-11]
2	(111) // (011)	[-110] // [-11-1]
3	(111) // (011)	[-101] // [-1-11]
4	(111) // (011)	[-101] // [-11-1]
5	(111) // (011)	[0-11] // [-1-11]
6	(111) // (011)	[0-11] // [-11-1]
7	(-111) // (011)	[-1-10] // [-1-11]
8	(-111) // (011)	[-1-10] // [-11-1]
9	(-111) // (011)	[0-11] // [-1-11]
10	(-111) // (011)	[0-11] // [-11-1]
11	(-111) // (011)	[101] // [-1-11]
12	(-111) // (011)	[101] // [-11-1]
13	(1-11) // (011)	[110] // [-1-11]
14	(1-11) // (011)	[110] // [-11-1]
15	(1-11) // (011)	[011] // [-1-11]
16	(1-11) // (011)	[011] // [-11-1]
17	(1-11) // (011)	[-101] // [-1-11]
18	(1-11) // (011)	[-101] // [-11-1]
19	(-1-11) // (011)	[1-10] // [-1-11]
20	(-1-11) // (011)	[1-10] // [-11-1]
21	(-1-11) // (011)	[101] // [-1-11]
22	(-1-11) // (011)	[101] // [-11-1]
23	(-1-11) // (011)	[011] // [-1-11]
24	(-1-11) // (011)	[011] // [-11-1]

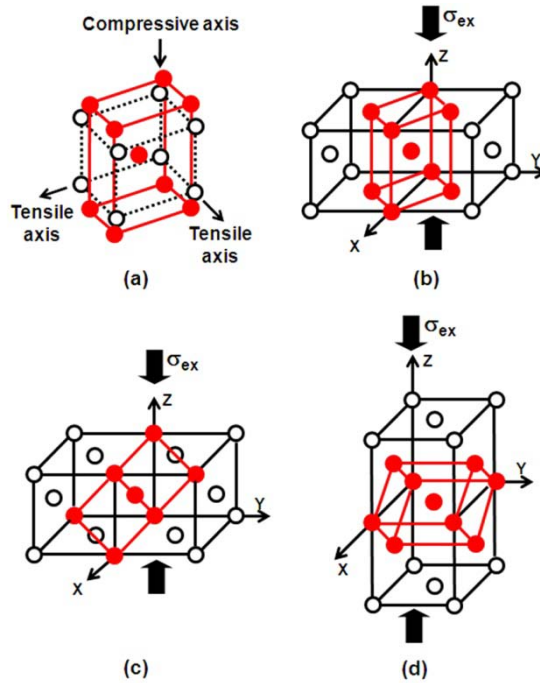


Figure 2.11. Schematic diagrams for Bain distortion. (a) Movement of crystal lattices for FCC-to-BCT transformation. Two tensile axes and one compressive axis are indicated. (b), (c) and (d) three different Bain variants depending on the direction of the compression axis. The variant whose compression axis for the Bain distortion is nearly parallel to the externally applied stress, σ_{ij} , has a higher probability of selection.

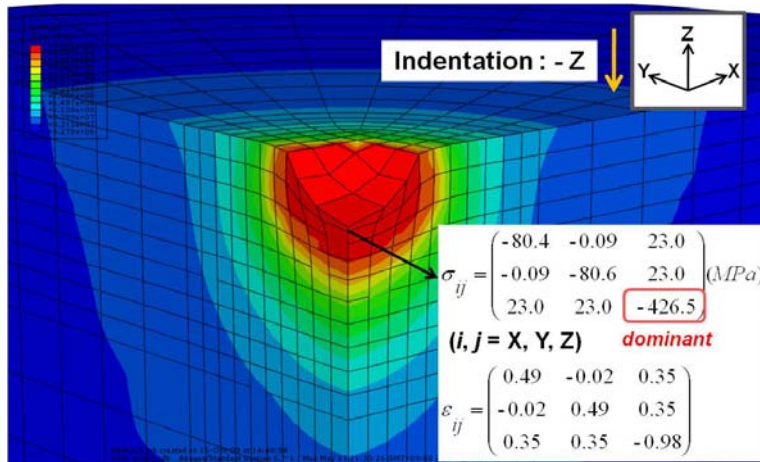


Figure 2.12. An FEM simulation for the von Mises stress and strain distribution underneath the indenter. Compressive stress along indentation axis, z, is dominant.

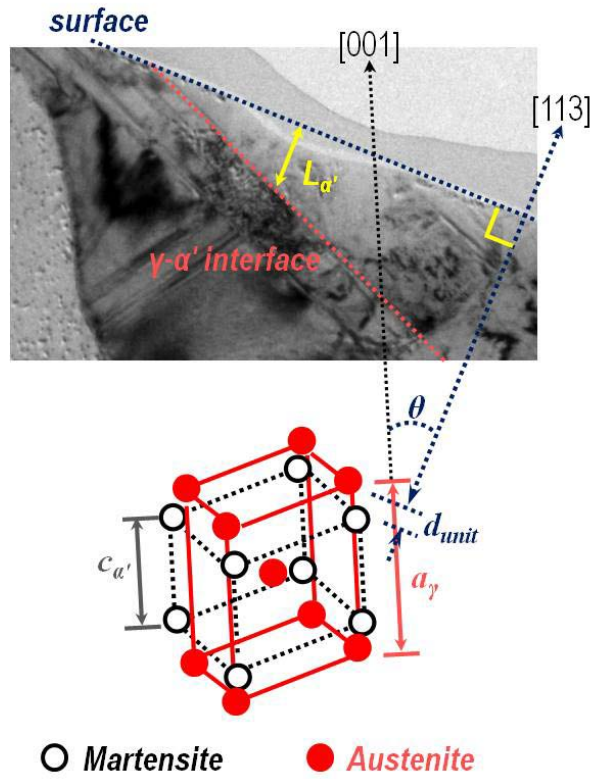


Figure 2.13. A schematic of crystal orientation and geometry with a cross-section TEM image underneath the indentation.

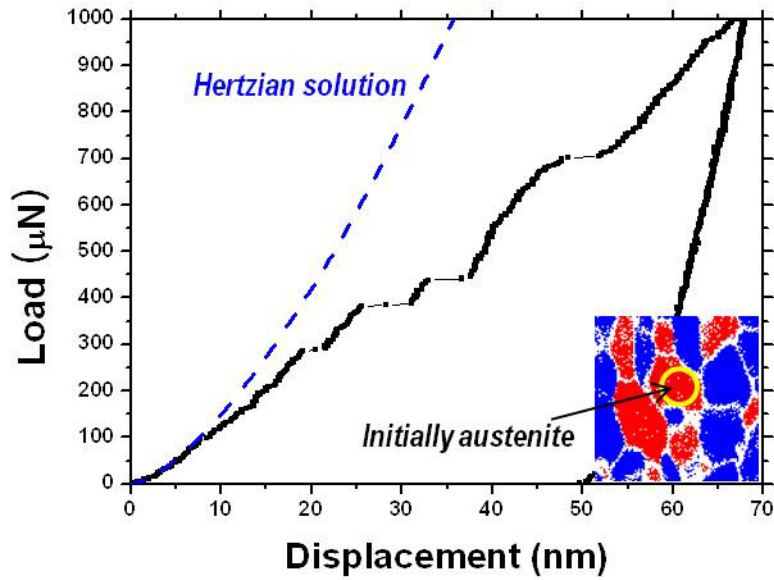
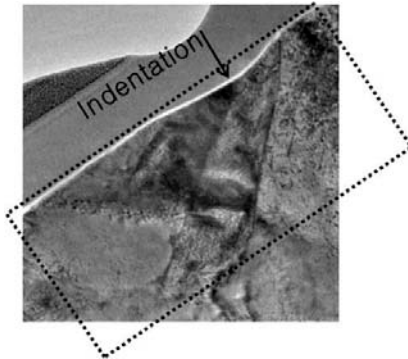


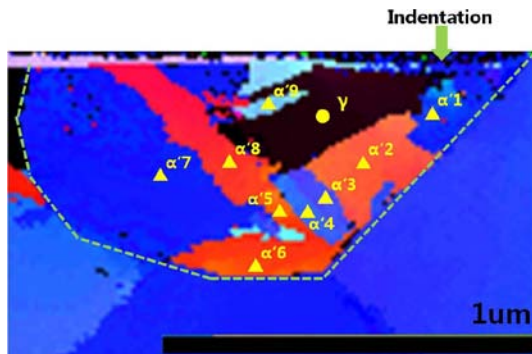
Figure 2.14. A load-displacement curve of a less stable austenite grain. The frequency of pop-in in a curve during plastic deformation was higher, compared to the steel in Figure 2.7.



(a)



(b)



(c)

Figure 2.15. (a) A TEM plan-view, (b) a phase map (Skyblue: BCC(BCT), Peach: FCC), (c) an orientation map measured by automatic TEM measuring system.

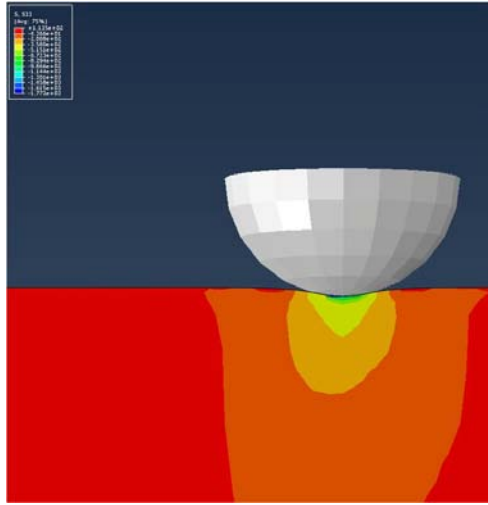


Figure 2.16. A computational simulation for the Cauchy stress distribution underneath the indenter using CP-FEM. The orientation which were measured by EBSD was used in the calculation.

Table 2.2. The measured and calculated K-S variants for each martensite under the indent. Top 4 favorable variants out of 24 from mechanical interaction energy calculation were listed in the table.

Position	Nearest K-S relationship (measured)		Max. U_i ,
	variant no.	misfit angle(°)	variant no.
$\alpha'1$	19	5.55	1,2, 19 ,20
$\alpha'2$	20	3.72	15,16,23,24
$\alpha'3$	21	1.06	15,16,23,24
$\alpha'4$	22	0.85	15,16,23,24
$\alpha'5$	23	2.40	15,16, 23 ,24
$\alpha'6$	23	1.67	15,16, 23 ,24
$\alpha'7$	14	4.03	15,16,23,24
$\alpha'8$	13	1.81	15,16,23,24
$\alpha'9$	24	3.61	15,16,23, 24

2.4. Appendix: Surface control for multiphase steel

Although nanoindentation has been recognized as the most appropriate method for nanoplasticity experiments, profound physical comprehension of the actual contact physics in the vicinity of indentation seems unclear yet due to the inhomogeneity of the surface properties [29]. For example, it is well known that the occurrence of pop-in can be dramatically reduced by mechanically altering the surface [22, 30-35]. Oliver and Pharr [30] showed that while pop-in occurs regularly on an electropolished tungsten surface, it is entirely eliminated when the surface is prepared by conventional mechanical polishing. Earlier studies of molecular dynamics also support these experimental investigations that the existence of surface step makes the pop-in load decrease significantly [36,37]. The conventional explanation for this is that, because mechanical polishing introduces dislocations in the near-surface region, plastic deformation can begin at much lower stresses by activation of pre-existing dislocations rather than nucleation of new ones [32,38,39]. Moreover, the increase of dislocation density on the material surface during sample preparation process even can result in the elevated hardness values as well, appropriate surface condition is essential for nanoindentation test.

Since the effect of the surface condition on the nanoindentation result is critical, there have been several experimental reports about the relationship

between various surface preparation methods and the initial pop-in behavior. Miyahara et al. [31] showed by means of etch pitting studies that altering the electropolished surfaces of tungsten single crystals by polishing with 0.05 μm alumina can increase the near surface dislocation density by several orders of magnitude, and that this totally eliminates the pop-in. Göken and Kempf [32] presented another possibility that mechanical polishing introduces steps on the contact surface that act as stress concentrators and reduce the loads needed for nucleation. More quantitative analyses were achieved by Shibutani et al. [40] that the rougher sample gives the lower pop-in load and the smoother sample is more sensitive to the local inhomogeneity in the vicinity of the surface. Lucca et al. [33] have shown that the surface condition for pop-in can be enhanced by chemically etching a surface prepared by colloidal silica polishing. And very recently, a systematic quantification for the influence of various surface preparation methods on nanoindentation pop-in has finally accomplished by Wang et al. Putting these various reports together, general conclusions on surface preparation methods are obtained. First, mechanical polishing, even polishing with very fine particle (0.05 μm alumina or diamond suspension), indeed introduces large amount of dislocations on the sample surface. Second, polishing with 0.02 μm colloidal silica, whose polishing action is based on chemical and mechanical process, reduces the damage but never fully removes. And finally, no other surface preparation methods but electropolishing can perfectly remove the mechanical polishing-induced

damaged layer.

However, despite of a simple conclusion to the surface preparation method for nanoindentation, electropolishing, there is another serious problem in preparing a sample if the material consists of two or more different phases those have different mechanical and chemical properties, such as multiphase TRIP steels in this study. Since a TRIP-aided multiphase steel consists of multiple phases with very different etching and polishing characteristics, it is hard to obtain a flat and smooth surface for each phase simultaneously. A flat and smooth surface is essential for both nanoindentation and EBSD which are the two key measuring systems for the selective nanoindentation exactly on the desired positions.

According to Zaefferer et al. [41], mechanically polished or chemically polished surface are not suitable and only an electropolished sample surface satisfies the condition for EBSD measurement of low-alloyed Al-added TRIP steels. However, result of electropolishing changes dramatically with the chemical composition and thermomechanical history of the TRIP steels, and also with electropolishing conditions. Therefore, in case of TRIP steel, suitable electropolishing conditions should be developed for sample by sample. Moreover, the metastable austenite at the sample surface can easily be transformed to martensite during mechanical polishing, carefully controlled treatment is essential for TRIP steels to obtain a flat, smooth, un-damaged and un-transformed surface with clearly exposed grain boundaries.

In this study, a variety of surface preparation methods were attempted and compared in order to find the most appropriate one that allows proper measurement for dual phase (ferrite+austenite) TRIP steels in both nanoindenter and EBSD system. Before applying each method, the samples were mechanically polished with SiC abrasive papers in the sequence of U.S. grit #320, #400, #600 and #800, followed by fine polishing on gentle and tender polishing clothes with diamond suspension of particle size from 6 μm down to 0.25 μm . After mechanical grinding and polishing, the samples underwent four different processes as final steps of surface treatment.

Figure 2.17 shows chemically etched surfaces of TRIP steel with a 3% nitric acid-97% methyl alcohol solution after mechanical polishing. Grain boundaries are clearly exposed and the surface inside each grain seems very flat and smooth as shown in Figure 2.17(a) and (c), an SEM and SPM scan image, respectively. However, an EBSD phase map (Figure 2.17(b)) shows that most of austenite phase at the surface had transformed to martensite during polishing and they were not removed by chemical etching at all. In the figure, only few FCC phase (red colored) were found and rest of the grains which should be FCC were unindexed, that means, they are martensite. Note that only the crystal informations for FCC austenite and BCC ferrite (blue colored) were used for indexing phases of the sample in EBSD. And also note that martensite is not easily indexed clear by EBSD due to its high dislocation density and often remains unindexed even though its crystal structure and

lattice parameters are very similar to ferrite in low-carbon steels. Therefore, the chemical etching is not suitable for measuring mechanical behaviors of austenite. Moreover, even though it looks flat and smooth inside the grains, it was flat only but surface roughness inside the grains was not actually fine for nanoindentation.

Figures 2.18 (a-c) are microstructures of electropolished surface. In this case, damaged layer at the surface with mechanical polishing-induced martensite were effectively removed and un-strained microstructures were revealed instead, which contains un-transformed retained austenite grains. However, it leads to a rather quick dissolution of austenite causing a strong surface relief, so austenite grains seem to be delicately picked out from the surface, as shown in Figure 2.18(a). The reason seems to be the different etching rates between ferrite and austenite. Therefore, this method, electropolishing only, can be said to be solely suitable for EBSD but nanoindentation never be able to be performed on this inhomogeneously etched surface.

Figure 2.19 shows the microstructures obtained after gentle polishing with 0.02 μm colloidal silica for 40 minutes followed by Ar^+ ion plasma etching. In this case, surface roughness and flatness inside the grains were outstanding and most of retained austenite grains were and revealed on the surface. Also, pop-in was detected almost every grains indented regardless of their phase, which means that the method reduces the damaged layer quite

effectively. However, some of polishing-induced martensite still remained on the surface and, moreover, sharp surface reliefs were also found at austenite grain boundaries. Therefore, colloidal silica polishing combined with Ar⁺ plasma etching is not regarded as a perfectly appropriate method, although the method reduces the damage at the surface quite effectively.

After a number of trial and errors for surface control of TRIP steel including those methods introduced above, it was concluded that the method should be finished with electropolishing as the final step while minimizing the difference in etching rate for each consisting phases. In order to meet these conditions, an attempt was made by repeating 3~7 times of extremely delicate polishing with #4000 U.S. grit SiC paper, chemical attack with a 4% HF-96% hydrogen peroxide solution and electropolishing with a 10% perchloric acid-90% ethyl alcohol solution in sequence. The result is a flat, smooth, unstained surface while austenite still remains untransformed, as the microstructures were already shown in Figure 2.4 and 2.5. Moreover, the difference in etching rate between phases can hardly be found in the figures, now austenite grains do not seem to be etched out any more, unlike when electropolished only. For the present dual phase TRIP steel, this sequential combination of polishing, etching and electropolishing is regarded as the most appropriate surface preparation method.

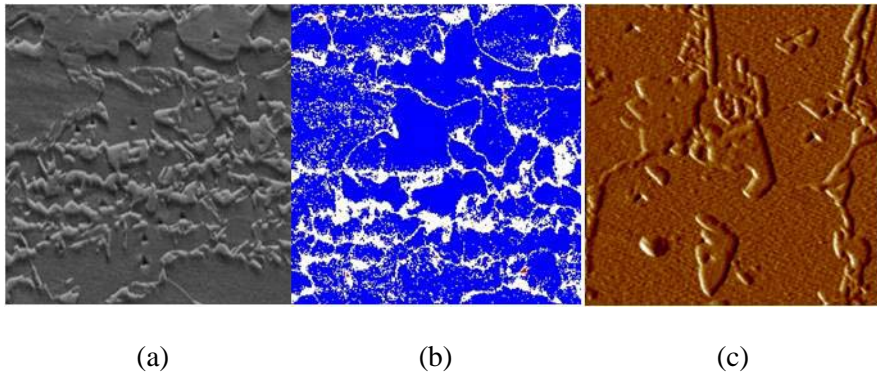
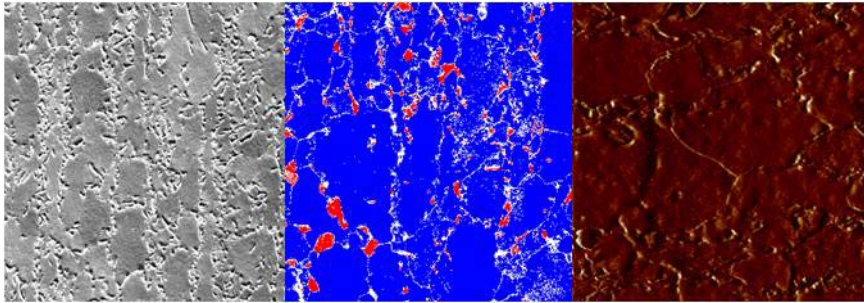


Figure 2.14. Microstructures of TRIP steel after chemical etching with a 3% nital solution. (a) SEM image, (b) EBSD phase map (blue: BCC, red: FCC, white: unindexed), (c) SPM scanning image.



(a)

(b)

(c)

Figure 2.15. Microstructures of TRIP steel after electropolishing. (a) SEM image, (b) EBSD phase map (blue: BCC, red: FCC, white: unindexed), (c) SPM scanning image.

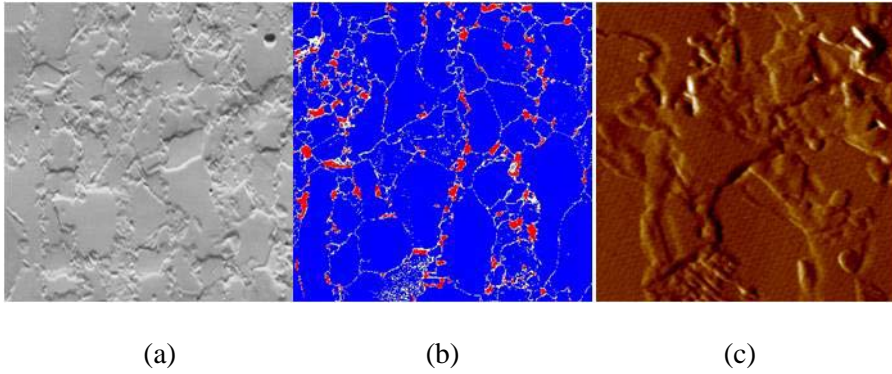


Figure 2.16. Microstructures of TRIP steel after colloidal silica polishing followed by Ar^+ plasma etching. (a) SEM image, (b) EBSD phase map (blue: BCC, red: FCC, white: unindexed), (c) SPM scanning image.

2.5. Conclusions

This study investigated the strain-induced phase transformation of individual metastable austenite grains in a TRIP steel using a combination of nanoindentation, EBSD, FIB and TEM. The load-displacement curve obtained from nanoindentation revealed two types of pop-in events on the loading segment. The first type was attributed to the elastic-to-plastic transition of austenite based on a Hertzian analysis of the elastic portion of the load-displacement curve. A second type of pop-in can be described as resulting from geometrical softening due to the selection of a favorable martensite variant based on the mechanical interaction energy between the externally applied stress and lattice deformation during nanoindentation. The existence of martensite after nanoindentation was confirmed by TEM analysis of the cross-section of an indented sample. The TRIP strain calculated by simple considering of crystal geometry change during phase transformation was in good agreement with the measured pop-in depth. Multiple pop-ins in less stable austenite was considered as a result of sequentially transformed multiple martensite from austenite.

2.6. References

- [1] G.B. Olson, M. Cohen : Metall. Trans. A, 1982, vol. 13, pp. 1907-1914.
- [2] S. Zaeferrer, J. Ohlert, W. Bleck : Acta Mater., 2004, vol. 52, pp. 2765-2778.
- [3] H.N. Han, C.-S. Oh, G. Kim, O. Kwon : Mater. Sci. Eng. A, 2009, vol. 499, pp. 462-468.
- [4] K.H.D.H. Bhadeshia : ISIJ Int., 2002, vol. 42, pp. 1059-1060.
- [5] H.N. Han, C.G. Lee, C.-S. Oh, T.-H. Lee, S.-J. Kim : Acta Mater., 2004, vol. 52, pp. 5203-5214.
- [6] K. Tao, H. Choo, H. Li, B. Clausen, J.-E. Jin, Y.-K. Lee : Appl. Phys. Lett., 2007, vol. 90, 101911.
- [7] K. Sugimoto, M. Kobayashi, S. Hashimoto : Metall. Mater. Trans. A, 1992, vol. 23, pp. 3085-3091.
- [8] Q. Furnémont, M. Kempf, P.J. Jacques, M. Göken, F. Delannay : Mater. Sci. Eng. A, 2002, vol. 328, pp. 26-32.
- [9] C.-S. Oh, D.-W. Suh, S.-J. Park, S.-J. Kim : J. Jpn. Soc. Heat Treatment, 2009, vol. 49, pp. 442-445.
- [10] H. Bei, Y.F. Gao, S. Shim, E.P. George, G.M. Pharr : Phys. Rev. B, 2008, vol. 77, 060103.
- [11] S. Shim, H. Bei, E.P. George, G.M. Pharr : Scr. Mater., 2008, vol. 59, pp. 1095-1098.

- [12] K.L. Johnson : *Contact Mechanics*, Cambridge Univ. Press, Cambridge, England, 1985, pp. 84-106.
- [13] A. Gouldstone, H.-J. Koh, K.-Y. Zeng, A.E. Giannakopoulos, S. Suresh : *Acta Mater.*, 2000, vol. 48, pp. 2277-2295.
- [14] J.J. Vlassak, W.D. Nix : *Philos. Mag. A*, 1993, vol. 67, pp. 1045-1056.
- [15] J.J. Vlassak, W.D. Nix : *J. Mech. Phys. Solids*, 1994, vol. 42, pp. 1223-1245.
- [16] D.N. Lee : *Texture and Related Phenomena*, The Korean Institute of Metals and Materials, Seoul, Korea, 2006, pp. 47-107.
- [17] A. Oila, S.J. Bull : *Comput. Mater. Sci.*, 2009, vol. 45, pp. 235-239.
- [18] R.W.K. Honeycombe : *Plastic Deformation of Metals*, second ed., Edward Arnold, London, England, 1984, pp. 33-35.
- [19] D. Hull, D.J. Bacon : *Introduction to Dislocations*, fourth ed., Elsevier Butterworth-Heinemann, Oxford, England, 2001, pp. 20.
- [20] H. Bei, Z.P. Lu, E.P. George : *Phys. Rev. Lett.*, 2004, vol. 93, 125504.
- [21] S.G. Corcoran, R.J. Colton : *Phys. Rev. B*, 1997, vol. 55, pp. R16057-R16060.
- [22] D.F. Bahr, D.E. Kramer, W.W. Gerberich : *Acta Mater.*, 1998, vol. 46, pp. 3605-3617.
- [23] H. Bei, E.P. George, J.L. Hay, G.M. Pharr : *Phys. Rev. Lett.*, 2005, vol. 95, 045501.
- [24] J.K. Mason, A.C. Lund, C.A. Schuh : *Phys. Rev. B*, 2006, vol. 73,

054102.

- [25] T. Ohmura, K. Tsuzaki : J. Phys. D, 2008, vol. 41, 074015.
- [26] G. Kurdjumov, G. Sachs : Z. Phys., 1930, vol. 64, pp. 325-343.
- [27] H.N. Han, D.-W. Suh : Acta Mater., 2003, vol. 51, pp. 4907-4917.
- [28] H.N. Han, C.G. Lee, D.-W. Suh, S.-J. Kim : Mater. Sci. Eng. A, 2008, vol. 485, pp. 224-233.
- [29] J.D. Kiely, R.Q. Hwang, J.E. Houston : Phs. Rev. Lett., 1998, vol. 81, pp. 4424-4427.
- [30] W.C. Oliver, G.M. Pharr : J. Mater. Res., 1992, vol. 7, pp. 1564-1583.
- [31] K. Miyahara, S. Matsuoka, N. Nagashima : JSME Int. J. Series A, 1998, vol. 41, pp. 562-568.
- [32] M. Göken, M. Kempf : Z. Metallkd., 2001, vol. 92, pp. 1061-1067.
- [33] D.A. Lucca, M.J. Klopstein, R. Ghisleni, G. Cantwell : Crip Annals- Manufacturing Technology, 2002, vol. 51, pp. 483-486.
- [34] J. Li, K.J. Van Vliet, T. Zhu, S. Yip, S. Suresh : Naure, 2002, vol. 418, pp. 307-310.
- [35] J.W. Yan, H. Takahashi, J. Tamaki, X.H. Gai, H. Harada, J. Patten : Appl. Phys. Lett., 2005, vol. 86, pp. 1-3.
- [36] C.L. Kelchner, S.J. Plimpton, J.C. Hamilton : Phys. Rev. B, 1998, vol. 58, pp. 11085-11088.
- [37] J.A. Zimmerman, C.L. Kelchner, P.A. Klein, J.C. Hamilton, S.M. Foils : Phys. Rev. Lett., 2001, vol. 87, 165507.

- [38] T.F. Page, W.C. Oliver, C.J. McHargue : J. Mater. Res., 1992, vol. 7, pp. 450-473.
- [39] Z. Wang, H. Bei, E.P. George, G.M. Pharr : Scripta Mater., 2011, vol. 65, pp. 469-472.
- [40] Y. Shibutani, A. Koyama : J. Mater. Res., 2004, vol. 19, pp. 183-188.
- [41] S. Zaefferer, P. Romano, F. Friedel : J. Microscopy, 2008, vol. 230, pp. 499-508.
- [42] M.S. Wechsler, D.S. Liberman, T.A. Reed : Trans. AIME, 1953, vol. 197, pp. 1503-1515.

Chapter 3

Relationship between ϵ martensite formation ($\gamma \rightarrow \epsilon$) and pop-in behavior in high nitrogen steel

3.1. Introduction

3.1.1. ϵ martensite in steel

In face-centered cubic (FCC) materials, stacking fault (SF) is one of the most important crystal imperfections introduced by deformation and plays a crucial role in subsequent plastic deformation [1,2]. At an initial stage of deformation, operation of Shockley partial dislocations forms the SF between the partials. The passage of Shockley partials along every second $\{111\}$ plane forms a hexagonal close-packed (HCP) structure (ϵ martensite) whereas introduction of Shockley partial dislocations on every successive $\{111\}$ plane produces a deformation twin [3–5]. As deformation proceeds, the ϵ martensite tends to transform into α' martensite, and the formation of strain-induced α' martensite has been of substantial interest owing to its favorable contribution to the work-hardening and ductility of steels, that is, TRIP effect [5].

The ϵ martensite transformation in steel have been extensively studied since Sato et al. first found in 1982 that Fe-Mn-Si based alloys exhibit an

excellent shape memory effect associated with reversible $\gamma \leftrightarrow \varepsilon$ phase transformation [6]. The well-known $\gamma \leftrightarrow \varepsilon$ transformation occurs by the introduction of stacking faults in each second close-packed plane of the FCC structure. Faults are created by motion of $a_\gamma/6\langle 112 \rangle$ Shockley partial dislocations, where a_γ is the lattice parameter of austenite. All $\{111\}$ close-packed planes lying in the FCC structure are possible shear planes. Each of them contains three $\langle 112 \rangle$ shear directions, therefore, there are 12 possible ε martensite variants. Crystallographic relationships between the two structures are $\{111\}_\gamma // \{0001\}_\varepsilon$, $\langle 110 \rangle_\gamma // \langle 1120 \rangle_\varepsilon$, which is known as the Shoji-Nishiyama (S-N) relationship [5].

Since there are three directions of Shockley dislocations exist in a compact plane, many different stackings can be imagined [7-10]. For instance, the three shear directions in a $\{111\}$ plane can be alternated in such a way that the shear strains of individual variants cancel each other out. This leads to a zero macroscopic shape change (Figure 3.1(a)), namely, “self-accommodated stacking”. Figure 3.1(b) shows another example of stacking that the displacement vectors of faulting are all the same, termed as “monopartial stacking.” This single shear direction stacking corresponds to the largest lattice shape change, the resulting shear of the HCP product is $1/(2\sqrt{2})$, i.e. an homogeneous shear of ~ 0.35 with a shear angle of 19.47° . Many studies report that thermal ε martensite appears in self-accommodated stackings form,

whereas stress-induced ϵ martensite appears in monopartial stackings form [7,11-21].

3.1.2. Stacking fault energy & deformation microstructure in high N steel

Nitrogen as an alloying element offers several beneficial effects on the properties of stainless steels, in particular those associated with good combination of mechanical properties and improved resistance to localized corrosion [22-24]. Owing to progresses in processing technologies, some commercial grades of high nitrogen steels (HNSs) are now available for industrial applications by utilizing carbon as a major alloying element together with nitrogen. According to Lee et al. [25], deformation mode gradually changed from strain-induced martensitic transformation to twinning-dominant deformation as nitrogen content increased.

A recent systematic investigation of correlation between stacking fault energy (SFE) and deformation microstructure in high interstitial alloyed austenitic steels [26] has shown that increase of interstitial elements content such as carbon and nitrogen increases SFE, and finally causes the change in deformation mode. According to the report, the deformation microstructure of austenitic Fe-18Cr-10Mn-N-C alloys can be classified into three categories: (i) strain-induced martensitic transformation (SIMT) in low SFE alloys (below $15 \text{ mJ}\cdot\text{m}^{-2}$), (ii) formation of deformation twin (DT) in high SFE alloys (above $20 \text{ mJ}\cdot\text{m}^{-2}$) and (iii) coexistence of SIMT and DT in intermediate SFE

alloys ($15\text{--}20 \text{ mJ}\cdot\text{m}^{-2}$). Figure 3.2 shows the proportional relationship between stacking fault energy and interstitial contents.

3.1.3. Motivations and objectives

Considering that the stress-induced ε martensite transformation is the predominant deformation mode in the early stage of plastic deformation and its monopartial nature, it is expected that geometrical softening can also occur if sufficient number of ε martensite bands form at the same time. Therefore, ε martensite transformation in the early stage of plastic deformation may be related to nanoindentation pop-in as well, just like α' martensite transformation is. In this chapter, nanoindentation and microstructural studies will be reported to provide experimental evidence of their relationship in metastable austenite in high nitrogen TRIP steel. Sequential experiments of EBSD, SPM, nanoindenter, FIB, and high resolution TEM (HR-TEM) were carried out to directly observe ε martensite under the indent.

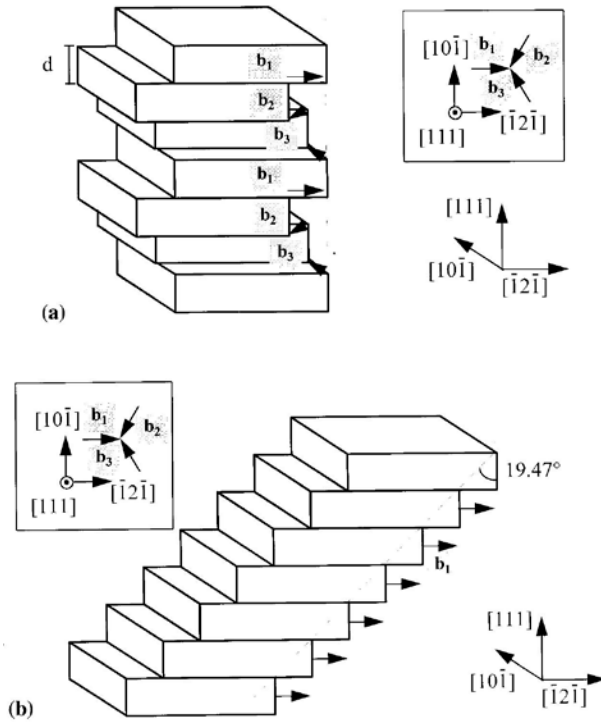


Figure 3.1. Examples of different dislocations stackings: (a) self-accommodated stacking, (b) monopartial stacking [8].

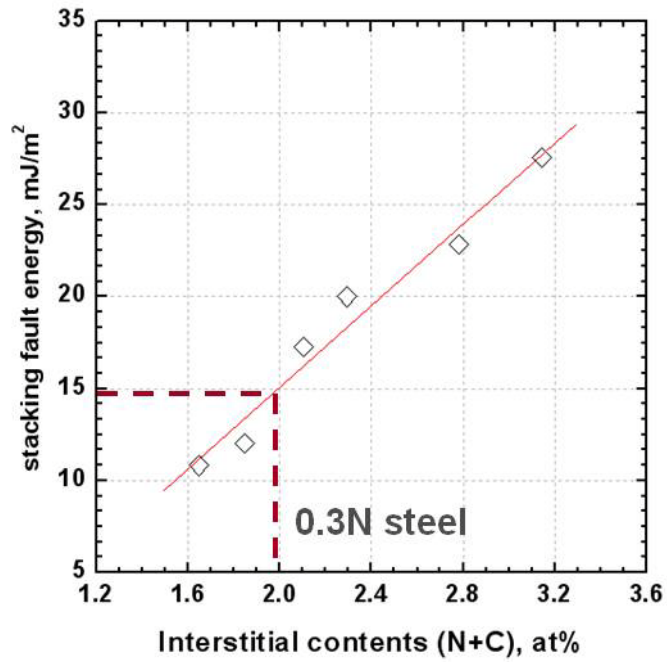


Figure 3.2. Relationship between stacking fault energy and interstitial contents [26]. The steel used in this study with 0.3wt% nitrogen content corresponds to stacking faults of about $15\text{mJ}\cdot\text{m}^{-2}$.

3.2. Experimental procedures

3.2.1. Sample preparation

The chemical composition of the high nitrogen TRIP steel used in this study was designed as Fe-0.02C-5.06Mn-0.19Si-0.23Ni-0.28N-20.08Cr (wt.%). With this composition, the stacking fault energy of austenite is approximately $15\text{mJ}\cdot\text{m}^{-2}$, which is known to have the initial deformation microstructure as ϵ martensite [26,27]. An EBSD system was used for the identification of phases, grains, orientations, and their boundaries on the flat surface. The specimens were prepared by a standard metallographic grinding and polishing procedure finishing with $0.25\mu\text{m}$ diamond suspension followed by electropolishing with a 10% perchloric acid-90% ethanol solution to remove the mechanically damaged layer. The average grain size of the austenite was approximately $15.6\ \mu\text{m}$, which is large enough to avoid interference by grain boundaries during nanoindentation.

3.2.2. Measuring procedure

After checking phases and locations of grains in the interested area by EBSD, nanoindentation tests were performed using a Hysitron TriboLab 750 Ubi nanoindentation system in load control at a constant loading rate of $400\mu\text{N/s}$ up to a maximum load of $2000\mu\text{N}$. A cono-spherical type indenter with a half angle of 30° was used. A scanning probe microscope (SPM) was

available in the system which made it possible to evaluate grain morphologies and identify precisely those areas that had been previously analyzed by EBSD. Figures 3.3(a) and (b) show an EBSD phase map and an orientation map obtained before nanoindentation, respectively. The circled austenite grain in the figures is the same as that at the center in an SPM image of the specimen surface after nanoindentation in Figure 3.3(c). Guided by the EBSD and SPM images, individual austenite grains were selected for nanoindentation after which the indented areas were analyzed again by SEM to determine if the indents lay entirely within single austenite grains. Cross section HR-TEM analysis of the indented specimen was performed to check for ϵ martensite in the region directly under the indent and to analyze the transformation defects geometrically. All TEM specimens examined in the present study were prepared on a focused Ga-ion beam (FIB) workstation (FEI Nova 200 Nanolab dual-beam FIB). Along the yellow dotted lines marked in Figure 3.3(c), cross-section lamellae, approximately 10 μm wide and 5 μm deep, were lifted out and attached to a Mo half-grid which fits in the TEM holder (Figure 3.3(d)). The prepared specimens were examined in a field-emission TEM (Tecnai G2 F30 S-Twin, FEI) operated at 300 keV (0.2 nm point-to-point resolution).

3.2.3. Determination of rotation angle in FIB

Since ϵ martensite and parent austenite have confined orientation

relationship (S-N relation: $\{111\}_\gamma // \{0001\}_\epsilon$, $\langle 110 \rangle_\gamma // \langle 1120 \rangle_\epsilon$), TEM zone axis must be aligned to $\langle 110 \rangle_\gamma // \langle 1120 \rangle_\epsilon$ in order to observe directly their orientational relationship and also the transformation defects (i.e., stacking faults by $a/6 \langle 112 \rangle_\gamma$ partial dislocations) in an edge-on view. A schematic representation of the monopartial formation of ϵ martensite via $\langle 110 \rangle_\gamma$ zone is shown in Figure 3.4. Therefore, cross-sectional FIB milling in a proper direction is essential to make the $\langle 110 \rangle_\gamma // \langle 1120 \rangle_\epsilon$ zone exist in the tilt angle limit of TEM. By rotating the bulk sample pertinently in FIB chamber, a TEM sample of which the thin plate is nearly perpendicular to $\langle 110 \rangle$ of austenite could be obtained. However, before rotating the sample, grains whose indentation direction is as perpendicular as possible to $\langle 110 \rangle_\gamma$ must be selected for cross-section sampling because this axis is always perpendicular to the electron beam direction in TEM, regardless of rotating angle in FIB.

The rotation angle in FIB which determines the direction of TEM sample normal can be calculated from the crystal orientation measured by EBSD. If the orientation of an austenite grain in bulk sample normal was measured (hkl), a plane $hx + ky + lz = d$ and the normal vector $\mathbf{p} = (h, k, l)$ can be imagined. When $\mathbf{r}_0 = (a, b, c)$ indicates one of $\langle 110 \rangle_\gamma$, the line vector \mathbf{r} which is parallel to \mathbf{p} and passes the point \mathbf{r}_0 is expressed as:

$$\mathbf{r} = \mathbf{r}_0 + t\mathbf{p} \quad (3.1)$$

By substituting Equation 3.1 to the equation of a plane, $\mathbf{p} \cdot \mathbf{r} = d$, t can be obtained:

$$t = \frac{d - \mathbf{p} \cdot \mathbf{r}_0}{\mathbf{p} \cdot \mathbf{p}} \quad (3.2)$$

Finally, the point \mathbf{r}_d , where the line vector \mathbf{r} meets the plane, becomes:

$$\mathbf{r}_d = \mathbf{r}_0 + \frac{d - \mathbf{p} \cdot \mathbf{r}_0}{\mathbf{p} \cdot \mathbf{p}} \mathbf{p} \quad (3.3)$$

Note that \mathbf{r}_d is the projection of a $\langle 110 \rangle_\gamma$ direction on the bulk sample surface. By cutting the sample along the direction perpendicular to \mathbf{r}_d as shown in Figure 3.3(c), a cross-sectional TEM sample whose normal of the thin plate is the most parallel to $\langle 110 \rangle_\gamma$, in the present case it is particularly $[\bar{1}10]_\gamma$, can be obtained.

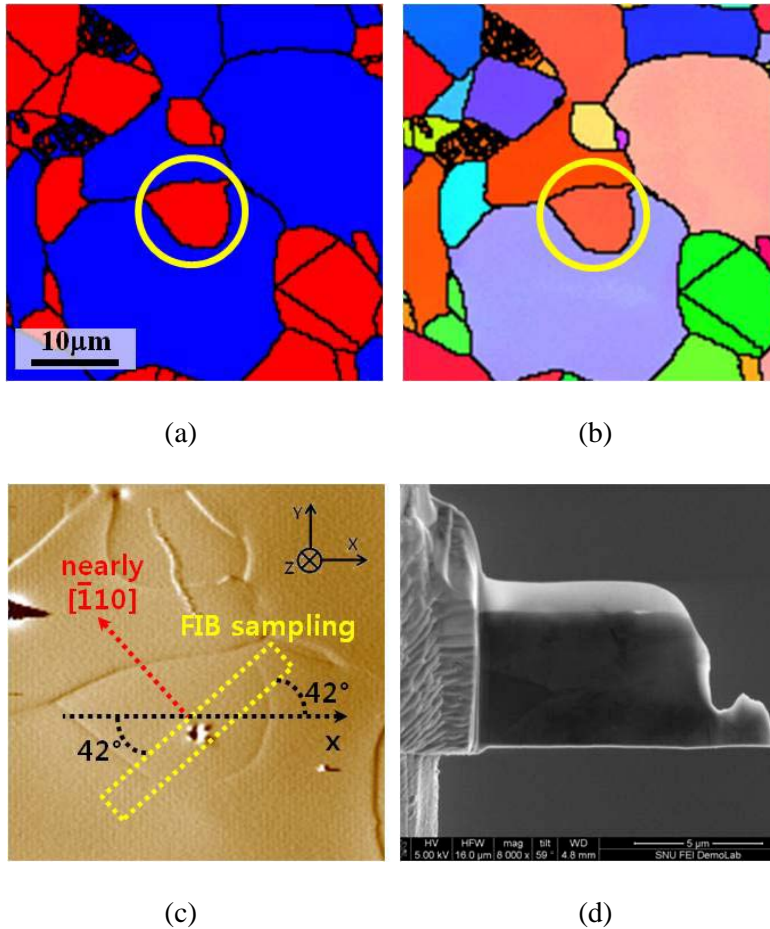


Figure 3.3. (a) EBSD phase map (Red: FCC, Blue: BCC), (b) orientation map of sample surface before indentation, (c) SPM image of indent in metastable austenite grain. Dotted yellow lines on SPM image showing schematically where FIB milling was used to cut out a cross-section through the indent for TEM analysis. (d) An FIBed cross-section sample is attached to a Mo half-grid for TEM.

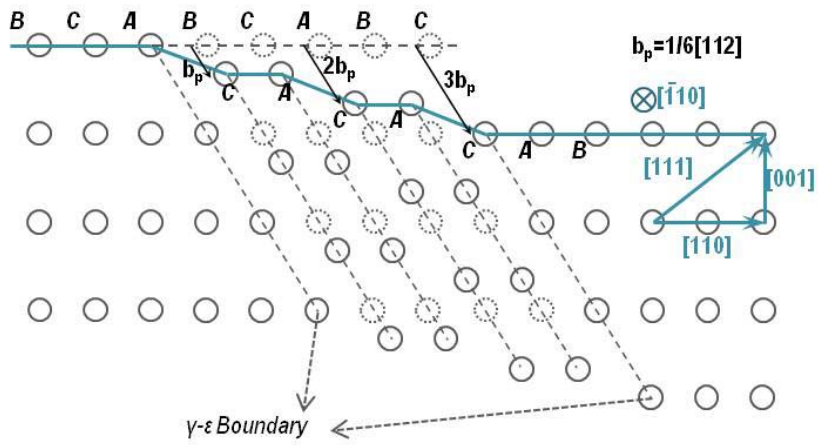


Figure 3.4. A schematic representation of the formation of monopartial ϵ martensite.

3.3. Results and discussion

First of all, the deformed microstructures of the steel were investigated by TEM analyses. Figure 3.5 shows the change of deformation microstructure of austenite as tensile strain increases. In the beginning, ϵ martensite is predominant and they transform to α' martensite as deformation proceeds. From an analysis of the diffraction patterns, ϵ and α' turned out to have S-N and N-W orientation relationship with parent austenite, respectively.

Figure 3.6 gives the load-displacement curve obtained by nanoindentation of the circled metastable austenite grain in Figure 3.3. Stepwise pop-ins were measured in the early stage of deformation. On carefully polished metal surfaces the deformation before the first pop-in has been shown to be perfectly elastic (e.g. [28,29]). Before the first pop-in, the initial elastic portion of the loading curves can be fitted to the Hertzian elastic contact solution [30] assuming that the indenter tip is spherical at shallow depths (Equations 1.2 and 1.7). The radius of our indenter tip was determined to be 663 nm from a calibration using standard fused quartz. Assuming isotropic elasticity, E_r can be calculated from the relation between the elastic constants of the sample and indenter. By substituting values of the room-temperature elastic constants of austenite ($E_s=199$ GPa and $\nu_s=0.29$) [31] and diamond ($E_i=1141$ GPa and $\nu_i=0.07$) into Equation 1.2, E_r was determined to be 182.58 GPa. Finally, the theoretical elastic behavior during indentation was

calculated using E_r and $R(=663 \text{ nm})$, and the results are plotted as the blue dashed lines in Figure 3.6. Before the first pop-ins, the experimental loading curves match the theoretical curve well, indicating elastic response before pop-in.

The maximum shear stress underneath the indenter, τ_m , can also be calculated from Hertzian analysis [30]. Using Equation 2.5, τ_m at pop-in ($\tau_{\text{pop-in}}$) for the annealed specimen was determined to be 5.29 GPa, which corresponds to $G/15$ where G , the shear modulus of austenite at room temperature, is 76.8 GPa [31]. The above value of $\tau_{\text{pop-in}}$ is within the range of values for the theoretical strength (τ_{th}) of a crystalline material [32], indicating that the pop-in in the annealed specimen are likely the result of dislocation nucleation.

In the present case, the pop-ins in the early stage of plastic deformation may be related to ϵ martensite transformation because stress-induced ϵ martensite transformation is the predominant deformation mode in the early stage of plastic deformation. Moreover, stress-induced ϵ martensite forms in monopartial stackings, which causes the largest lattice shape change, geometrical softening is expected if a sufficient number of ϵ martensite bands form at the same time. To check for the presence of ϵ martensite in the indented region, the cross-section of a sample indented was examined by TEM. Figure 3.7 shows a plan-view image of the cross-section sample, there

is an obvious indent on the surface and deformed regions under the indent. From an analysis of the diffraction patterns (Figure 3.8), the region close to the indent (marked as A) consisted of two phases, transformed α' martensite and the parent austenite. Because region A corresponds to the highly stressed zone by nanoindentation [33,34], severe deformation must have been introduced in the region. Therefore, it is considered that in region A, austenite had already transformed to α' martensite by large amount of strain, which corresponds to microstructure of 40% tensile deformation in Figure 3.5.

Region B is about 900nm away from the center of the indent, where it is considered that less stress was applied than region A. Figure 3.9(a) shows a high resolution image of region B from $[\bar{1}10]_{\gamma}$ zone, there are many thin parallel bands lying in the same direction (marked as a dotted line in the figure) distributed all through the examined area. From analyses of this lattice image and the numerical diffractogram of the image, this banded structure turned out a lamellar structure consisting of a mixture of ϵ and γ phases. Figure 3.9(b) is a closer look of Figure 3.9(a), showing a juxtaposition of (111) planes of γ austenite and (0001) planes of ϵ martensite clearly. Although thickness of single lamellae of each phase was only a few planes, this fine banded structure was observed through a wide range. A diffractogram obtained by fourier transformation of the high resolution image also presents the existence of both γ and ϵ phases (Figure 3.9(c)). From analysis of the

diffraction patterns, $(111)_\gamma$ and $(0001)_\epsilon$ were indexed at the same position, indicating the S-N orientation relationship between FCC austenite and HCP martensite. The particular orientation of austenite out of 24 equivalent systems caused by cubic symmetry was determined by comparing the planes and directions in the high resolution image to the orientation of the bulk sample that had been previously measured by EBSD.

In metals, plastic deformation initiates on a certain slip system that has the greatest resolved shear stress by given external stress. According to this rule, known as Schmid's law [35], the critical stress required to cause yielding is a function of $\cos\Phi\cos\lambda$ or the Schmid factor:

$$\tau = \sigma \cos\phi \cos\lambda \quad (3.4)$$

where τ is the resolved stress on a slip system, σ is the uniaxial stress applied from external, Φ is the the angle between the slip plane normal and and the stress axis, and λ the angle between the slip direction and the stress axis, respectively. According to the equation above, a slip system with the greatest resolved shear stress acting upon it will predominate in the slip process. In the present study, the Schmid factors of 12 equivalent Shockley partial dislocations were calculated in order to identify the most favorable direction of monopartial ϵ martensite formation. It was assumed that the stress which

was caused by indentation was nearly uniaxial compression (Figure 2.12), and the indentation axis was perfectly normal to the sample surface. As shown in the Table 3.1, it was calculated that $(111)[11\bar{2}]$ slip system has the greatest absolute value of Schmid factor among the 12 variants of partial slip, indicating that this slip system is the the most favorable one for slip to occur on. This slip system $(111)[11\bar{2}]$, which is predicted to be the predominant one for slip, is the same slip system that experimentally observed by EBSD-TEM (Figure 3.9), suggesting that the ϵ martensite bands beneath the indent were formed by nanoindentation-induced stress.

The lattice displacement along the indentation axis by formation of ϵ martensite was also calculated. If the displacement vectors of faulting are all the same (i.e., monomartial stackings), the resulting shear of ϵ martensite is $1/(2\sqrt{2})$ [8-10]. Considering that the stacking faults in every other (111) plane makes ϵ martensite, the lattice displacement in one HCP plate along $[11\bar{2}0]$ direction becomes $2a_\gamma/\sqrt{6}$ ($= 2b_p$ in Figure 3.4). The lattice parameter of austenite, a_γ , was determined to be approximately 0.32nm from TEM results. Then, the unit displacement along the indentation axis when one ϵ martensite plate forms from austenite, d_i , could be simply obtained by considering the angle between the partial direction and the indentation axis, λ in Equation 3.4:

$$d_i = \left| \frac{2a_\gamma}{\sqrt{6}} \cos \lambda \right| \quad (3.5)$$

The results for all 12 variants are listed in Table 3.1. The unit displacement along indentation axis for (111)[11 $\bar{2}$] slip system, which is the one that both ideally favorable and experimentally examined, was calculated 0.16 nm. Note that the values in Table 3.1 are the displacement made by formation of only one ϵ martensite plate, which is denoted by $2b_p$ in Figure 3.4. Therefore, it can be easily imagined that if only over 10 ϵ martensite layers were made at the same moment, the amount of displacement along the indentation axis will be an order of several nanometers, which could be detected as pop-in. In the high resolution image in Figure 3.9, over twenty of thin ϵ martensite bands were observed in such a small area of only about 20 nm \times 20 nm. Because all the ϵ bands in the figure are lying monopartially, they possibly have introduced several nanometers of pop-in if they were formed at the same time. Moreover, it is so fair that the cluster of this lamellar structure should be wider than the observed area, suggesting that the number of thin ϵ martensite lamellae should be more. Therefore, it is considered that stress-induced ϵ martensite transformation had contributed to the occurrence of pop-in in the early stage of plastic deformation. Remember that the stacking fault energy of the material used in this study was about 15mJ \cdot m $^{-2}$, that is, the predominant

deformation mode in the early stage of plastic deformation is expected to be the formation of ϵ martensite [26,27]. Together, these microstructural observations strongly suggest that the pop-in behavior in the early stage of plastic deformation of austenite is closely related to the formation of ϵ martensite.

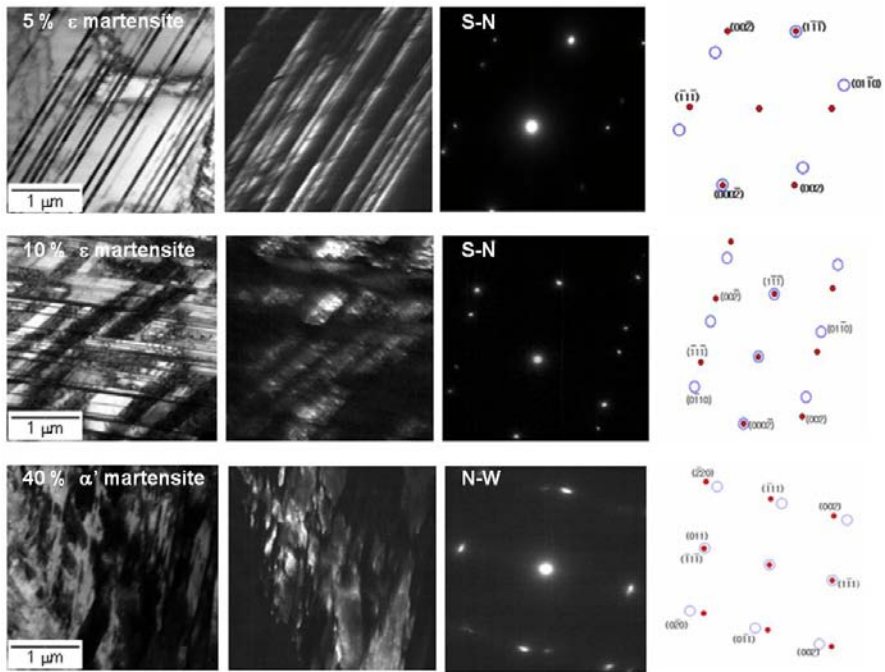


Figure 3.5. Microstructure change in austenite as tensile deformation increases.

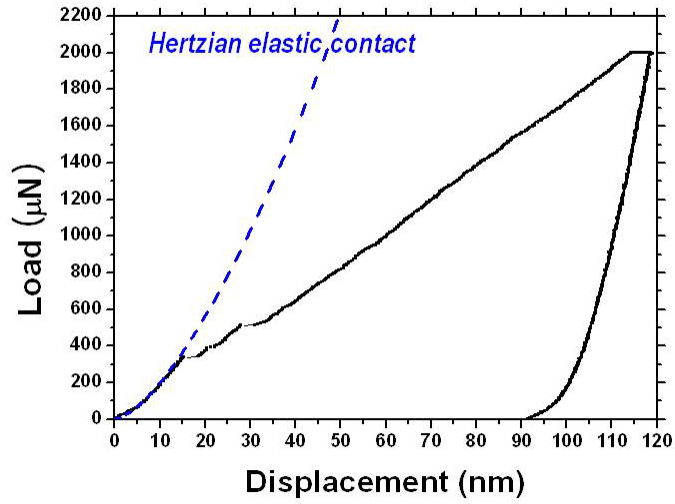


Figure 3.6. Load-displacement curve obtained by nanoindentation of the metastable austenite grain.

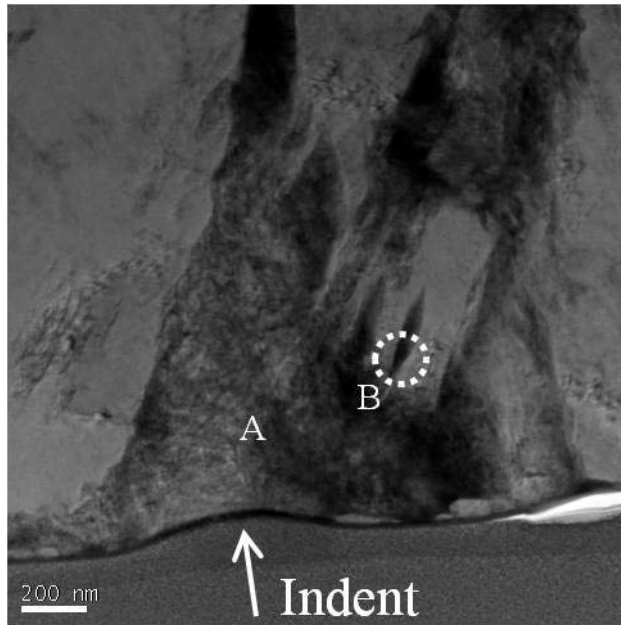


Figure 3.7. A plan-view image of the cross-section sample, there is an obvious indent on the surface and deformed regions under the indent.

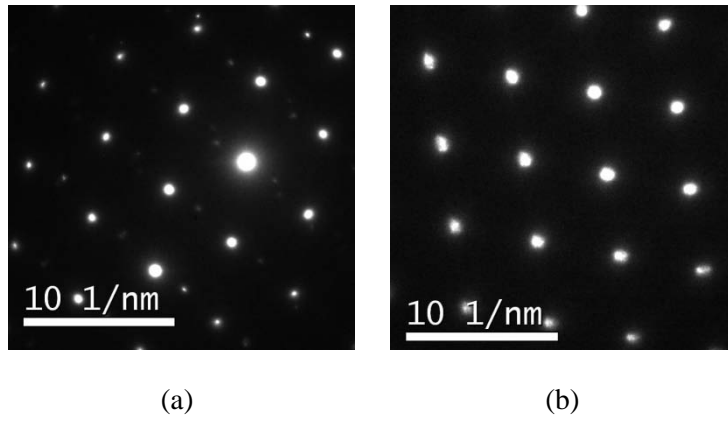
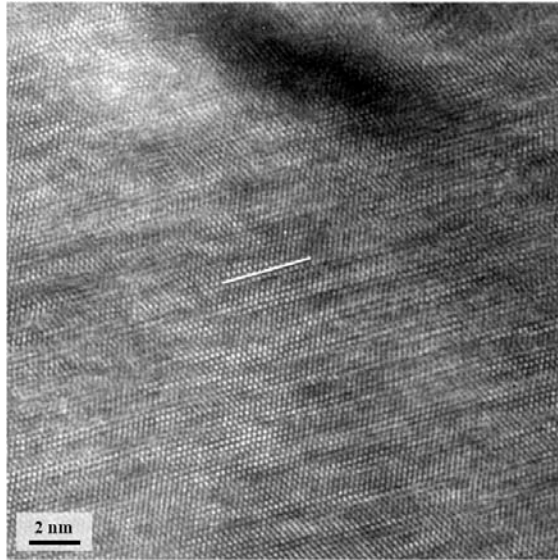
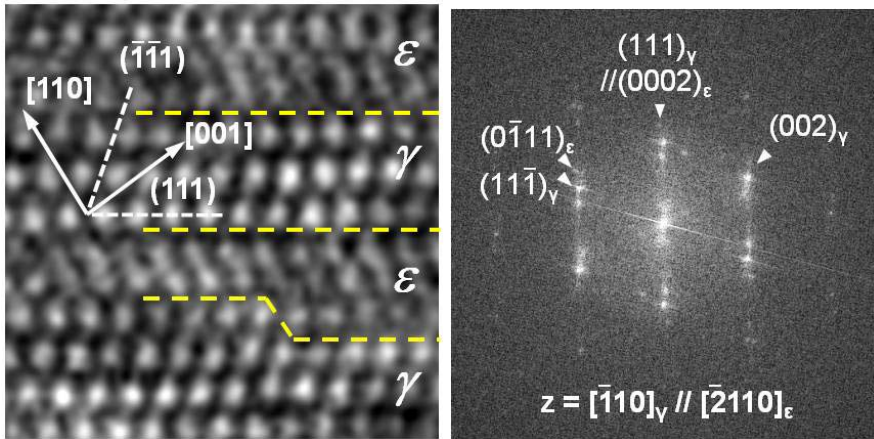


Figure 3.8. Diffraction patterns obtained around region A in Figure 3.6. Both (a) $\langle 111 \rangle \alpha'$ and (b) $\langle 110 \rangle \gamma$ were found in region A.



(a)



(b)

(c)

Figure 3.9. (a) A high resolution image of region B (zone= $[\bar{1}10]_{\gamma}$). (b) A closer look of (a). The image was rotated 15° in clockwise for easier view of the lattices. (c) A numerical diffractogram obtained by FFT of (a).

Table 3.1. Schmid factor and the unit displacement along indentation axis, d_i , for 12 variants of Shockley partial movement.

Slip plane	Partial direction	Schmid factor	d_i (nm)
(111)	[11-2]	-0.483	0.16
(111)	[1-21]	0.324	0.11
(111)	[-211]	0.158	0.05
(-111)	[1-12]	0.384	0.22
(-111)	[12-1]	-0.090	0.05
(-111)	[211]	0.294	0.17
(-1-11)	[112]	0.315	0.24
(-1-11)	[-121]	0.121	0.09
(-1-11)	[2-11]	0.194	0.15
(1-11)	[-112]	0.464	0.19
(1-11)	[121]	0.381	0.15
(1-11)	[21-1]	-0.083	0.03

3.4. Conclusions

This study investigated the relationship between pop-in behavior of austenite in the early stage of nanoindentation and formation of ϵ martensite based on microstructural analyses. Sequential experiments of EBSD, SPM, nanoindenter, FIB, and high resolution TEM (HR-TEM) were carried out to directly observe ϵ martensite under the indent. The load-displacement curve obtained from nanoindentation revealed stepwise pop-ins in the early stage of plastic deformation. Considering that the stress-induced ϵ martensite transformation is the predominant deformation mode in the early stage of plastic deformation and its monopartial nature as well, geometrical softening can also occur by ϵ martensite formation. From analyses of high resolution TEM images, a cluster of banded structure under the indent turned out a juxtaposition of (111) planes of γ austenite and (0001) planes of ϵ martensite. The most favorable slip system predicted by simple calculations based on the Schmid's law was the same one that experimentally observed by TEM. It was also calculated that formation of more than just 10 single ϵ martensite layers in this slip system can introduce several nanometers of pop-in. These microstructural investigations strongly suggest that the pop-in behavior in the early stage of plastic deformation of austenite is closely related to the formation of ϵ martensite.

3.5. References

- [1] B.E. Warren : *X-ray diffraction*, Dover Publications Inc, New York, 1990.
- [2] C.N.J. Wagner : Analysis of the broadening and change in position of peaks in an X-ray powder pattern. In: Cohen JB, Hilliard JE, editors. Local atomic arrangement studied by X-ray diffraction. Gordon and Breach, New York, 1966, p. 219.
- [3] J.W. Christian, S. Mahajan : *Prog. Mater. Sci.*, 1995, vol. 39, pp. 1-157.
- [4] L.J. Teutonico : *Acta Metall.*, 1963, vol. 11, pp. 1283-1289.
- [5] Z. Nishiyama : *Martensitic transformation*, Academic Press Inc., New York, 1971.
- [6] A. Sato, E. Chishima, K. Soma, T. Mori : *Acta metal.*, 1982, vol. 30, pp. 1177-1183.
- [7] J.H. Yang, C.M. Wayman : *Mat. Charact.*, 1992, vol. 28, pp. 23-35.
- [8] N. Bergeon, G. Guenin, C. Esnouf : *Mater. Sci. Eng. A*, 1997, vol. 238, pp. 309-316.
- [9] N. Bergeon, G. Guenin, C. Esnouf : *Mater. Sci. Eng. A*, 1998, vol. 242, pp. 77-86.
- [10] N. Bergeon, S. Kajiwara, T. Kikuchi : *Acta Mater.*, 2000, vol. 48, pp. 4053-4064.
- [11] J.H. Yang, C.M. Wayman : *Mater. Charact.*, 1992, vol. 28, pp. 37-47.

- [12] J.L. Putaux, J.P. Chevalier : Acta Mater., 1996, vol. 44, pp. 1701-1716.
- [13] T. Maki, K. Tsuzaki : Proc. Int. Conf. Martensitic Transformations, Monterey, CA, USA, 1992, Monterey Institute for Advanced Studies, Monterey, 1993, pp. 1151.
- [14] A. Sato, E. Chishima, Y. Yamaji, T. Mori : Acta Metall., 1984, vol. 32, pp. 539-547.
- [15] H. Fujita, S. Ueda : Acta Metall., 20 (1972) 759-767.
- [16] E. Delamotte, C. Altstetter : TMS AIME, 1969, vol. 245, pp. 651-659.
- [17] A. Seeger : Z. Metallkd., 1953, vol. 44, pp. 247-253.
- [18] A. Seeger : Z. Metallkd., 1956, vol. 47, pp. 653-660.
- [19] W. Bollman : Acta Metall., 1961, vol. 9, pp. 972-975.
- [20] S. Mahajan, M.L. Green, D. Brasen : Metall. Trans. A, 1977, vol. 8, pp. 283-293.
- [21] L.I. Lysak : Fiz. Metal. Metall. 20 (1967) 547.
- [22] V.G. Gavriljuk, H. Berns : *High Nitrogen Steels*, Springer-Verlag, Berlin, 1999, pp. 1.
- [23] M.O. Speide : In: Foct J, Hendry A, editors. High nitrogen steel 88, Lille, France, 18–20 May 1988, The Institute of Metals, London, 1989, pp. 92.
- [24] T.-H. Lee, C.-S. Oh, S.-J. Kim, S. Takaki : Acta Mater., 2007, vol. 55, pp. 3649-3662.

- [25] T.-H. Lee, C.-S. Oh, S.-J. Kim : *Scripta Mater.*, 2008, vol. 58, pp. 110-113.
- [26] T.-H. Lee, E. Shin, C.-S. Oh, H.-Y. Ha, S.-J. Kim : *Acta Mater.*, 2010, vol. 58, pp. 3173-3186.
- [27] K. Sekido, T. Ohmura, T. Sawaguchi, M. Koyama, H.W. Park, K. Tsuzaki : *Scripta Mater.*, 2011, vol. 65, pp. 942-945.
- [28] H. Bei, Y.F. Gao, S. Shim, E.P. George, G.M. Pharr : *Phys. Rev. B*, 2008, vol. 77, 060103.
- [29] S. Shim, H. Bei, E.P. George, G.M. Pharr : *Scr. Mater.*, 2008, vol. 59, pp. 1095-1098.
- [30] K.L. Johnson : *Contact Mechanics*, Cambridge Univ. Press, Cambridge, England, 1985, pp. 84-106.
- [31] D.N. Lee : *Texture and Related Phenomena*, The Korean Institute of Metals and Materials, Seoul, Korea, 2006, pp. 47-107.
- [32] R.W.K. Honeycombe : *Plastic Deformation of Metals*, second ed., Edward Arnold, London, England, 1984, pp. 33-35.
- [33] H. Bei, Z.P. Lu, E.P. George : *Phys. Rev. Lett.*, 2004, vol. 93, 125504.
- [34] H. Bei, E.P. George, J.L. Hay, G.M. Pharr : *Phys. Rev. Lett.*, 2005, vol. 95, 045501.
- [35] E. Schmid, W. Boas : *Kristalplastizitat*, Springer and Hughes, Berlin and London, 1950.

Chapter 4

Relationship between yield drop and nanoindentation pop-in behavior of steel

4.1. Introduction

Recently, nanoindentation has been employed to probe small-scale mechanical properties which are relevant to a wide range of materials and applications. The response of a material to nanoindentation is usually presented in the form of a load-displacement curve. When metallic materials undergo irreversible permanent deformation, discrete physical events, such as dislocation nucleation [1-18], dislocation source activation [14,15], phase transformation [16,19-30], and mechanically-induced twinning [31,32], can be detected as discontinuities on nanoindentation load-displacement curves. Among these, we consider here just the onset of plasticity resulting from dislocation nucleation or dislocation source activation which can produce geometrical softening accompanied by a sudden displacement excursion in the very early stage of mechanical contact during load-controlled nanoindentation, an event referred to in the literature as a “pop-in.”

Geometrical softening can also occur as a result of yield point phenomena manifested as yield drops followed by propagation of Lüders

strain in the early part of the tensile stress-strain curves of body-centered cubic metals. A mechanism for this was first proposed by Cottrell [33] wherein dislocations that are trapped by solute atmospheres break free simultaneously at the upper yield point and multiply, causing instantaneous softening and a sharp yield drop. Figure 4.1 shows a schematic of Cottrell atmosphere and corresponding tensile behaviors. Then, when the load is removed after plastic deformation and the specimen allowed to rest, the solute atoms diffuse to the dislocations as time passes, a process that can occur even at room temperature in the case of relatively mobile solutes such as interstitial carbon atoms. This causes the dislocations to be locked-up again by the solute atoms, resulting in a decrease in the mobile dislocation density and a reappearance of the yield point, a phenomenon that is referred to as strain aging [33]. Schematic diagrams in Figure 4.2 well describe the strain aging phenomenon [34].

Because both pop-ins during nanoindentation and yield drops during tensile testing are manifestations of strain softening, they may be related to each other at a fundamental level despite their very different length scales. In this chapter, experimental evidence of their close relationship in a ferritic steel will be provided by investigating mechanical responses at the macro- and nano- scales using tensile testing and nanoindentation, respectively.

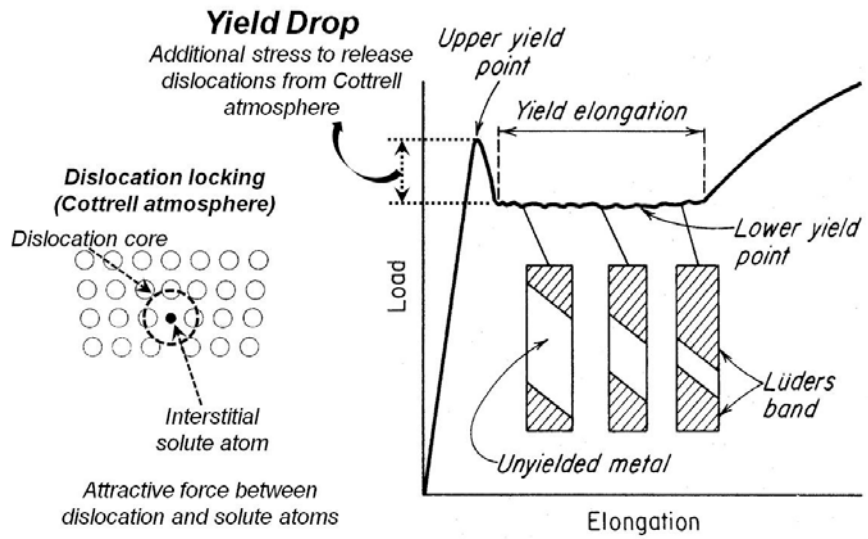


Figure 4.1. A schematic of Cottrell atmosphere and corresponding tensile behaviors [33].

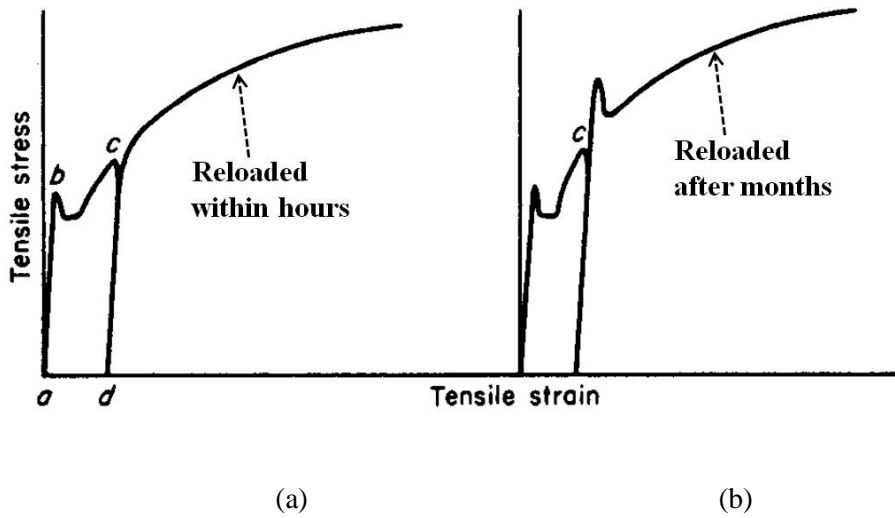


Figure 4.2. Strain aging. (a) Load removed from specimen at point *c* and specimen reloaded within a short period of time (hours). (b) Load removed at point *c* and specimen reloaded after a long period of time (months) [34].

4.2. Experimental procedures

The material used in this study was a cold-rolled plate of a ferritic steel with the chemical composition Fe-0.06C-0.08Si-0.16Mn-0.02Al-0.0006N-0.01Cr (wt.%) that was fully annealed at 1053K. An electron backscattered diffraction (EBSD) system (HKL Nordlys Channel 5) was used for the identification of phases, grains, orientations, and their boundaries on polished surfaces. The specimens were prepared by a standard metallographic grinding and polishing procedure finishing with 0.25 μ m diamond suspension followed by electropolishing with a 10% perchloric acid-90% ethanol solution to remove the mechanically damaged layer. The volume fractions of the phases were determined to be approximately 99% ferrite and 1% pearlite, based on optical microscopy images and the combined band contrast and slope map [35-37] obtained from EBSD measurements, as shown in Figure 4.3 and Figure 4.4(a), respectively. The average grain size of the ferrite was 21 μ m, which is large enough to avoid interference by grain boundaries during nanoindentation.

Macroscopic deformation behavior was investigated by uniaxial tensile tests at a constant extension rate of 1mm·min⁻¹ using plate-type ASTM standard subsize specimens [38]. Initially, the specimens were loaded to 6% nominal strain and unloaded. Then the specimens were strain aged for various times at room temperature and reloaded to determine the aging time at which

the yield point reappeared.

Nanoindentations were made using a Hysitron Tribolab nanoindentation system operated in load-control at a constant loading rate of $200\mu\text{Ns}^{-1}$ up to a maximum load of $1000\mu\text{N}$. A Berkovich type indenter with a half angle of 65.3° was used. In order to investigate the relationship between pop-in behavior and yield point phenomena, four sets of tests were performed: just before, right after, 30 hours after, and 3 weeks after the 6% tensile pre-strain. For each of these conditions, a total of 64 indentations were made in an 8×8 array with $4\mu\text{m}$ spacing between the indents, as shown in Figure 4.4. Based on the EBSD band contrast map and SPM images, only those indentations that were located in the ferrite grains far enough away from the grain boundaries were selected for analyses in order to exclude any grain boundary effect on the load-displacement curves [11,39,40].

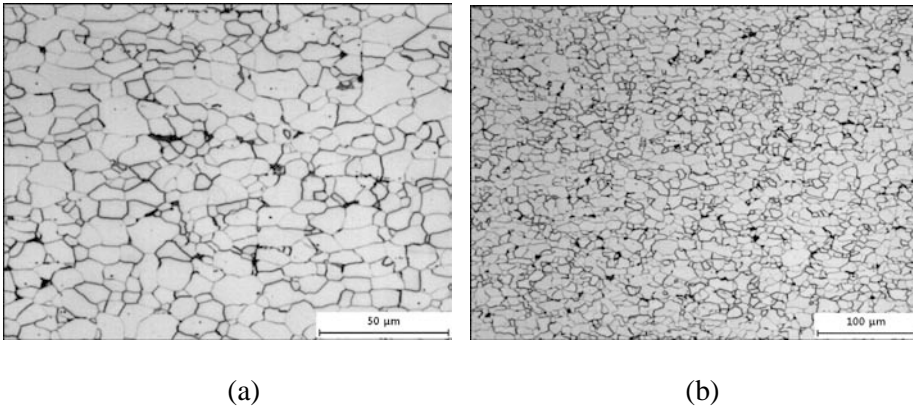
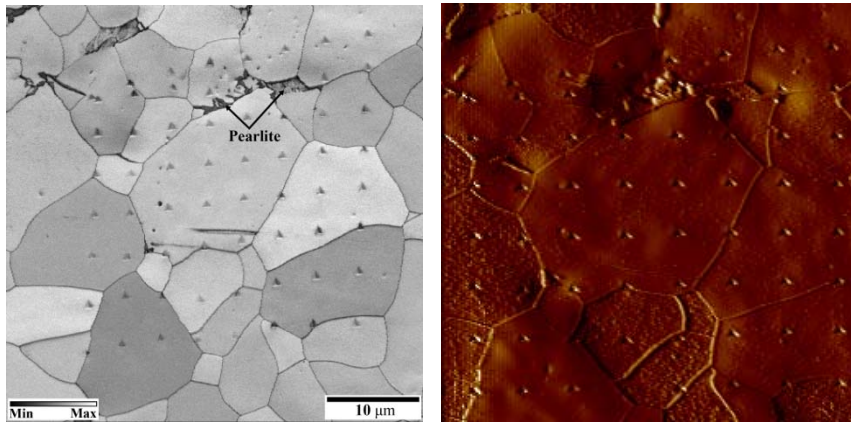


Figure 4.3. Microstructure of the ferritic steel by an optical microscope. (a) $\times 200$, (b) $\times 500$.



(a)

(b)

Figure 4.4. (a) A combined EBSD band contrast and slope map and (b) an SPM image for the fully annealed steel specimen showing majority ferrite grains, isolated (~1%) pearlite colonies, and an 8x8 array of indentations. Only those indents that were located squarely within the ferrite grains and away from the boundaries were analyzed in the present study.

4.3. Results and discussion

Figure 4.5 presents the stress-strain curves obtained from uniaxial tensile tests of the steel. For the fully annealed specimen, a sharp yield point is clearly observed. After the initial elastic portion, a significant yield drop occurred at the upper yield point, followed first by Lüders strain propagation and then uniform elongation accompanied by work hardening. In the case of specimens that were deformed to 6% nominal strain, unloaded, and then reloaded, their behavior depended on the strain aging time. When reloaded right after unloading, the material did not show a clear yield drop, as shown in Figure 4.5(a). In contrast, a sharp yield point was observed when the specimen was reloaded after 30 hours of strain aging, as shown in Figure 4.5(b). These results are typical of yield point phenomena seen in steels.

Interestingly, similar behaviors were also observed in the nanoindentation tests. Figures 4.6(a-d) show the load-displacement curves for nanoindentations performed before, right after, 30 hours after, and 3 weeks after 6% pre-strain. Before the pre-strain (i.e., annealed state), large and obvious pop-ins were observed on the loading curves for most of the indentations at quite high loads (100~700 μ N), as shown in Figure 4.6(a). In this study, a sudden displacement excursion larger than 3nm was defined as a pop-in. Before the first pop-in, the initial elastic portion of the loading curves can be fitted to the Hertzian elastic contact solution [41] assuming that the

indenter tip is spherical at shallow depths (Equations 1.2 and 1.7). The radius of the indenter tip R was determined to be $1\mu\text{m}$ from a calibration using standard fused quartz. Assuming isotropic elasticity, E_r can be calculated from the relation between the elastic constants of the sample and indenter. By substituting values of the room-temperature elastic constants of ferrite ($E_s=208.2\text{GPa}$ and $\nu_s=0.29$) [42] and diamond ($E_i=1141\text{GPa}$ and $\nu_i=0.07$) into Equation 1.2, E_r was determined to be 189.7GPa . Finally, the theoretical elastic behavior during indentation was calculated using E_r and $R(=1\mu\text{m})$, and the results are plotted as the blue dashed lines in Figure 4.6. Before the first pop-ins, the experimental loading curves match the theoretical curve well, indicating elastic response before pop-in. Additionally, a linear relationship between the pop-in start load and the amount of burst was well established as shown in Figure 4.7, which is in consistent with earlier reports [11,43] on the pop-in as a signal for incipient plasticity.

The maximum shear stress underneath the indenter, τ_m , can also be calculated from Hertzian analysis [41]. Using Equation 2.5, τ_m at pop-in ($\tau_{\text{pop-in}}$) for the annealed specimen was determined to be in the range $3.3\sim 5.3\text{GPa}$, which corresponds to $G/25\sim G/15$ where G , the shear modulus of ferrite at room temperature, is 80.7GPa [42]. These values of $\tau_{\text{pop-in}}$ are within the range of values for the theoretical strength (τ_{th}) of a crystalline material [44], indicating that the pop-ins in the annealed specimen are likely the result of

dislocation nucleation. Based on a total of 14 indents that were located squarely within the ferrite grains, the average value of $\tau_{\text{pop-in}}$ for the annealed steel was found to be 3.96 ± 0.92 GPa (Table 4.1), which corresponds to $\sim G/20$. Similar results were obtained previously for annealed Ni single crystals [14], where it was found that the pop-in stresses during nanoindentation with small radius spheres were in the range of the theoretical strength ($\sim G/14$). Note that, although the average $\tau_{\text{pop-in}}$ values are comparable to the theoretical strength, there are indent-to-indent variations, which may be due to thermal fluctuations [13,45] or surface imperfections [46,47].

However, the orientation effect on the pop-in start load is worth being checked because the pop-in stress could also vary with crystal orientation, which alters the angle between the Burgers vector and the indentation axis grain by grain [11]. If the variation of pop-in load is a result of crystal orientation, simply we can consider that the pop-in load should be in proportion to the Taylor factor of each grain. By applying the strain field generated underneath the indenter (Figure 2.12) to the grain orientations measured from EBSD (Figure 4.8(a)), a Taylor factor map could be obtained for the grains tested, as shown in Figure 4.8(b). But as shown in Figure 4.9(a), the pop-in start load had no strong dependency on the calculated Taylor factor, namely, the grain orientation. The distribution of pop-in start loads in one grain shown in Figure 4.9(b) shows it more clearly that the crystal orientation is not a

decisive factor in determining the pop-in stress. These results are consistent with an earlier report [2] that no orientational dependence for the yield point is because of the large dependence of the yield point on the surface roughness. Therefore, statistical approach would be a suitable method for the pop-in load analysis.

Figure 4.6(b) shows representative load-displacement curves for nanoindentation tests performed right after the pre-strain. No distinct pop-in was observed on any of these curves. Instead, most of the curves showed only a slight change of slope without a clear pop-in to mark the onset of plasticity. The transition loads were relatively low, less than $100\mu\text{N}$, indicating elastic-plastic deformation practically right from the start of indentation in the pre-strained specimen.

Figures 4.6(c) and (d) show the nanoindentation load-displacement curves obtained 30 hours and 3 weeks after the pre-strain, respectively. In both cases, distinct pop-ins reappeared for some of the indentations, while they were never observed when the specimen was indented right after the pre-strain. Moreover, as shown in Figures 4.6(b-d), the pop-in loads increased with increasing strain aging time.

For the pop-in loads shown in Fig. 4.6, the maximum shear stresses under the indenter ($\tau_{\text{pop-in}}$) were calculated as discussed earlier. Figure 4.10 shows these calculated pop-in stresses (average values ± 1 standard deviation)

for the annealed, pre-strained, and strain-aged conditions. The annealed specimen pops-in at the theoretical strength, consistent with the notion that plastic deformation of dislocation-free volumes requires nucleation of dislocations. After 6% tensile pre-strain, however, the pop-ins disappear, indicating that, if there are enough mobile dislocations in the stressed volume, plastic deformation can occur by movement of these pre-existing dislocations at very low loads (essentially right from the start of deformation) rather than by the nucleation of new dislocations at very high stresses. These results are consistent with earlier results which showed that the frequency of pop-in occurrence can be dramatically reduced by mechanically altering the surface [3,48], that is, as a result of dislocation-induced damage. Similarly, it has been shown that the pop-in stresses decreased with increasing pre-strain and indenter size [14] suggesting that it is easier to activate pre-existing dislocations than it is to nucleate new ones [7,21]. As has been discussed before, pop-in loads depend on the initial dislocation density in the highly stressed zone underneath the indenter [14,15]. If the density of the pre-existing mobile dislocations is high and the radius of the spherical indenter tip is much larger than the dislocation spacing, movement of dislocations will, in general, occur at lower applied stresses than those needed for dislocation nucleation, resulting in lower values for the pop-in stresses.

What has not been investigated until now is the effect of interstitial solute atoms on pop-in behavior. At the macroscopic scales of tensile tests,

the origin of the sharp yield point is known to be dislocation locking by interstitial solute atoms, the so-called Cottrell atmosphere [33]. In order to free a dislocation from this atmosphere, additional stress over that normally required for dislocation movement is needed resulting in a sharp yield drop after the dislocations break free and multiply. We find here that an analogous situation exists in the case of nanoindentation where the softening is manifested as a pop-in. Immediately after the 6% pre-strain, the steel has a high density of new dislocations which are relatively mobile because they have not yet been pinned by the solute atoms. Therefore, both the sharp yield points (Figure 4.5(a)) and the distinct pop-ins (Figure 4.6(a)) disappear. However, when the solute atoms diffuse to the dislocations as the aging time increases, they tend to anchor the dislocations again, which results in a recovery of the yield point phenomenon (Figure 4.5(b)). When a nanoindentation is made near a location where the dislocations are pinned, a higher stress is needed to unlock them. This causes a reappearance of the pop-in (clear elastic-to-plastic transition). Additionally, if we assume that the longer the strain aging time, the higher the probability of making an indent near a pinned dislocation, then it stands to reason that the pop-ins would occur more frequently as well as at higher loads with increasing aging time, as shown in Figure 4.6(d). Together, these nanoindentation and tensile test results strongly suggest that the pop-in behavior in ferrite is closely related to its yield point phenomenon.

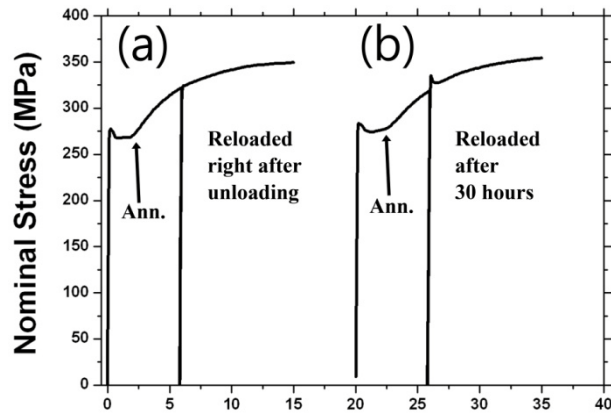


Figure 4.5. Comparison of the uniaxial tensile stress-strain curves for the annealed steel specimen (arrows) with those obtained after (a) loading to 6% strain, unloading, and then immediately reloading and (b) loading to 6% strain, unloading, strain aging for 30 hours, and then reloading. The curves in (b) are offset from the origin for clarity of presentation.

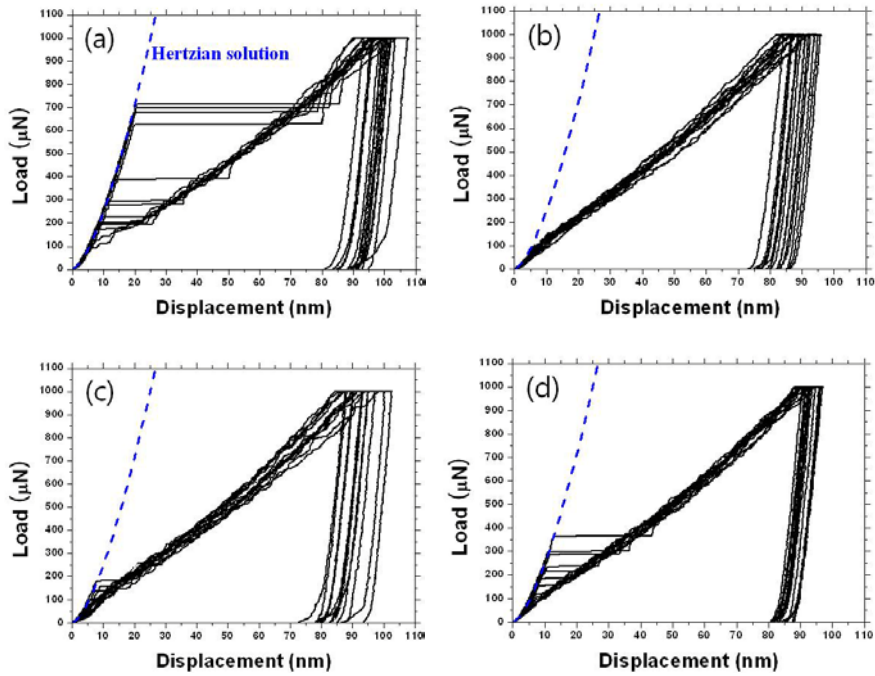


Figure 4.6. Nanoindentation load-displacement curves obtained (a) before, (b) right after, (c) 30 hours after and (d) 3 weeks after 6% tensile pre-strain. In (a), (c) and (d) the experimental data (black lines) before the pop-ins match well the theoretical Hertzian elastic contact solution (blue dashed lines). In (b) the deformation is elastic-plastic practically right from the start.

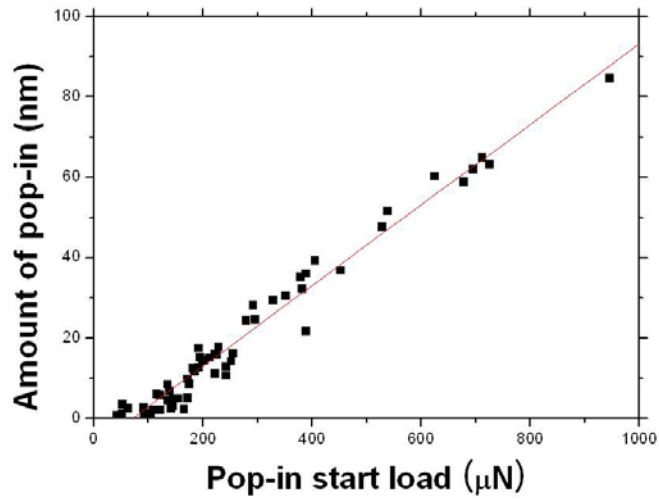
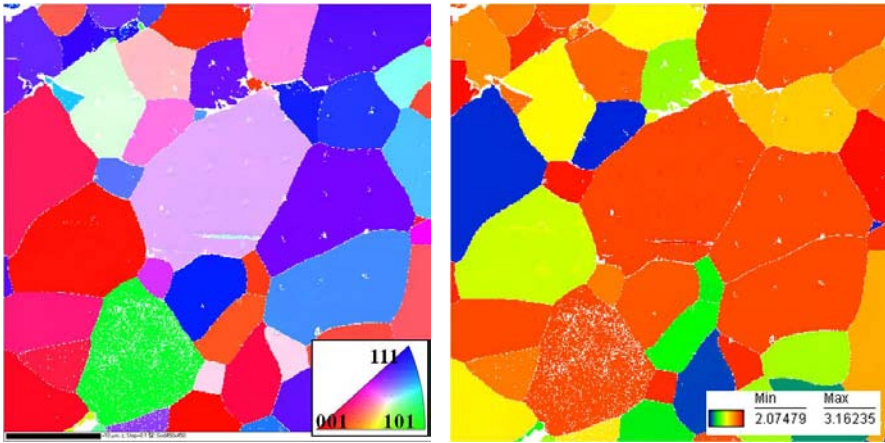


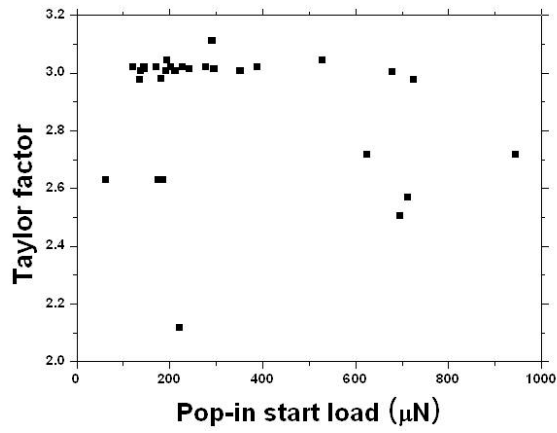
Figure 4.7. A linear relation between the pop-in load and the amount of pop-in.



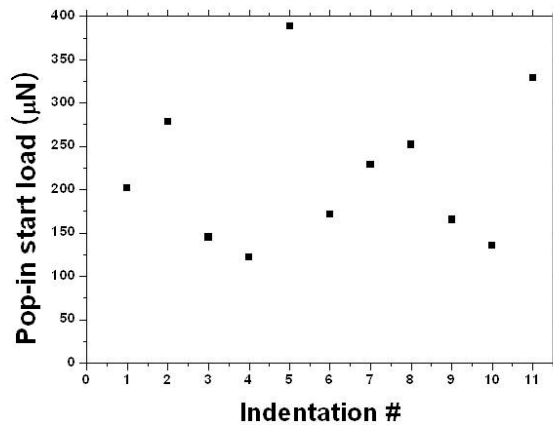
(a)

(b)

Figure 4.8. (a) An orientation map (ND) and (b) a corresponding Taylor factor map.



(a)



(b)

Figure 4.9. (a) Relationship between Taylor factor and the pop-in start load. (b) Distribution of pop-in start load in one grain.

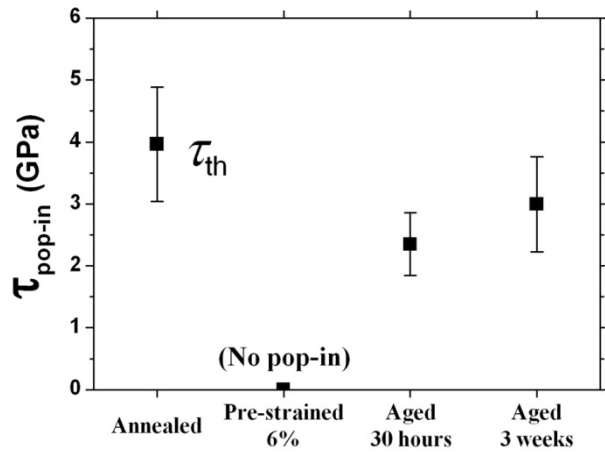


Figure 4.10. Nanoindentation pop-in stresses before, right after, 30 hours after, and 3 weeks after the 6% tensile prestrain.

Table 4.1. Maximum shear stress at pop-in in ($\tau_{\text{pop-in}}$) for annealed, pre-strained and strain aged conditions. No distinct pop-in was observed on pre-strained specimen.

Condition	Average (GPa)	Maximum (GPa)	Minimum (GPa)	Standard Deviation (GPa)	# of indents
Annealed	3.96	5.29	2.67	0.92	14
Pre-strained 6%	-	-	-	-	15
Aged 30 hours	2.35	3.33	1.66	0.51	14
Aged 3 weeks	3.00	4.22	1.65	0.76	15

4.4. Conclusions

This study investigated the relationship between pop-in behavior during nanoindentation and yield point phenomena in tensile tests by comparing the mechanical responses of pre-strained and strain-aged ferritic steel. The pop-ins observed on the load-displacement curves of the annealed specimens (i.e., before tensile pre-straining), were attributed to dislocation nucleation based on Hertzian analyses. Their disappearance right after pre-straining and reappearance after strain aging, similar to the disappearance and reappearance of yield drops in tensile tests, strongly suggest that nanoindentation pop-ins in ferritic steel are closely related to their yield points. Both phenomena are influenced by dislocation locking by solutes (Cottrell atmospheres).

4.5. References

- [1] W.W. Gerberich, J.C. Nelson, E.T. Lilleodden, P. Anderson, J.T. Wyrobek : *Acta Mater.*, 1996, vol. 44, pp. 3585-3598.
- [2] S.G. Corcoran, R.J. Colton, E.T. Lilleodden, W.W. Gerberich : *Phys. Rev. B.*, 1997, vol. 55, pp. R16057-R16060.
- [3] D.F. Bahr, D.E. Kramer, W.W. Gerberich : *Acta Mater.*, 1998, vol. 46, pp. 3605-3617.
- [4] C.L. Kelchner, S.J. Plimpton, J.C. Hamilton : *Phys. Rev. B*, 1998, vol. 58, pp. 11085-11088.
- [5] E.B. Tadmor, R. Miller, R. Phillips, M. Ortiz : *J. Mater. Res.*, 1999, vol. 14, pp. 2233-2250.
- [6] A. Gouldstone, H.-J. Koh, K.-Y. Zeng, A.E. Giannakopoulos, S. Suresh : *Acta Mater.*, 2000, vol. 48, pp. 2277-2295.
- [7] M. Göken, M. Kempf : *Z. Metallkd.*, 2001, vol. 92, pp. 1061-1067.
- [8] A. Gouldstone, K.J. Van Vliet, S. Suresh : *Nature*, 2011, vol. 411, pp. 656.
- [9] E.T. Lilleodden, J.A. Zimmerman, S.M. Foiles, W.D. Nix : *J. Mech. Phys. Solids*, 2003, vol. 51, pp. 901-920.
- [10] H. Bei, E.P. George, J.L. Hay, G.M. Pharr : *Phys. Rev. Lett.*, 2005, vol. 95, 045501.
- [11] T. Ohmura, K. Tsuzaki : *J. Mater. Sci.*, 2007, vol. 42, pp. 1728-1732.

- [12] A.A. Zbib, D.F. Bahr : Metall. Mater. Trans. A., 2007, vol. 38, pp. 2249-2255.
- [13] H. Bei, Y.F. Gao, S. Shim, E.P. George, G.M. Pharr : Phys. Rev. B, 2008, vol. 77, 060103(R).
- [14] S. Shim, H. Bei, E.P. George, G.M. Pharr : Scripta Mater., 2008, vol. 59, pp. 1095-1098.
- [15] A. Barnoush, M.T. Welsch, H. Vehoff : Scripta Mater., 2010, vol. 63, pp. 465-468.
- [16] T.-H. Ahn, C.-S. Oh, D.H. Kim, K.H. Oh, H. Bei, E.P. George, H.N. Han : Scripta Mater., 2010, vol. 63, pp. 540-543.
- [17] S.M. Han, T. Bozorg-Grayeli, J.R. Groves, W.D. Nix : Scripta Mater., 2010, vol. 63, pp. 1153-1156.
- [18] C. Begau, A. Hartmaier, E.P. George, G.M. Pharr : Acta Mater., 2011, vol. 59, pp. 934-942.
- [19] G.M. Pharr, W.C. Oliver, D.R. Clarke : Scripta Metall., 1989, vol. 23, pp. 1949-1952.
- [20] G.M. Pharr, W.C. Oliver, D.S. Harding : J. Mater. Res., 1991, vol. 6, pp. 1129-1130.
- [21] T.F. Page, W.C. Oliver, C.J. McHargue : J. Mater. Res., 1992, vol. 7, pp. 450-473.
- [22] D.L. Callahan, J.C. Morris : J. Mater. Res., 1992, vo. 7, pp. 1614-1617.
- [23] E.R. Weppelmann, J.S. Field, M.V. Swain : J. Mater. Res., 1993, vol. 8,

- pp. 830-840.
- [24] E.R. Weppelmann, J.S. Field, M.V. Swain : J. Mater. Sci., 1995, vol. 30, pp. 2455-2462.
- [25] H.N. Han, D.-W. Suh : Acta Mater., 2003, vol. 51, pp. 4907-4917.
- [26] H.N. Han, C.G. Lee, C.-S. Oh, T.-H. Lee, S.-J. Kim : Acta Mater., 2004, vol. 52, pp. 5203-5214.
- [27] J.-I. Jang, M.J. Lance, S. Wen, T.Y. Tsui, G.M. Pharr : Acta Mater., 2005, vol. 53, pp. 1759-1770.
- [28] H.N. Han, C.-G. Lee, D.-W. Suh, S.-J. Kim : Mater. Sci. Eng. A., 2008, vol. 485, pp. 224-233.
- [29] H.N. Han, C.-S. Oh, G. Kim, O. Kwon : Mater. Sci. Eng. A., 2009, vol. 499, pp. 462-468.
- [30] M.-G. Lee, S.-J. Kim, H.N. Han : Int. J. Plas., 2010, vol. 26, pp. 688-710.
- [31] J.E. Bradby, J.S. Williams, J. Wong-Leung, M.V. Swain, P. Munroe : Appl. Phys. Lett., 2002, vol. 80, pp. 2651-2653.
- [32] R.D.K. Misra, Z. Zhang, Z. Jia, M.C. Somani, L.P. Karjalainen : Scripta Mater., 2010, vol. 63, pp. 1057-1060.
- [33] A.H. Cottrell : *Dislocations and Plastic Flow in Crystals*, Oxford Univ. Press, London, England, 1953, pp.139-150.
- [34] R.E. Reed-Hill, R. Abbaschian : *Physical Metallurgy Principles*, 3rd ed., PWS publishing company, Boston, USA, 1994, pp. 288.

- [35] T.-H. Ahn, K.-K. Um, J.-K. Choi, D.H. Kim, K.H. Oh, M. Kim, H.N. Han : *Mater. Sci. Eng. A*, 2009, vol. 523, pp. 173-177.
- [36] J.Y. Kang, D.H. Kim, S.-I. Baik, T.-H. Ahn, Y.-W. Kim, H.N. Han, K.H. Oh, H.-C. Lee, S.H. Han : *ISIJ Int.*, 2011, vol. 51, pp. 130-136.
- [37] Y.M. Kim, T.-H. Ahn, K.K. Park, K.H. Oh, H.N. Han : *Met. Mater. Int.*, 2011, vol. 17, pp. 181-186.
- [38] ASTM : E 8-00, Standard Test Methods for Tension Testing of Metallic Materials.
- [39] W.A. Soer, K.E. Aifantis, J.Th.M. De Hosson : *Acta Mater.*, 2005, vol. 53, pp. 4665-4676.
- [40] E.T. Lilleodden, W.D. Nix : *Acta Mater.*, 2006, vol. 54, pp. 1583-1593.
- [41] K.L. Johnson : *Contact Mechanics*, Cambridge Univ. Press, Cambridge, England, 1985, pp. 84-106.
- [42] D.N. Lee : *Texture and Related Phenomena*, The Korean Institute of Metals and Materials, Seoul, Korea, 2006, pp. 47-107.
- [43] Y. Shibutani, A. Koyama : *J. Mater. Res.*, 2004, vol. 19, pp. 183-188.
- [44] R.W.K. Honeycombe : *Plastic Deformation of Metals*, second ed., Edward Arnold, London, England, 1984, pp. 33-35.
- [45] C.A. Schuh, A.C. Lund : *J. Mater. Res.*, 2004, vol. 19, pp. 2152-2158.
- [46] W.W. Gerberich, S.K. Venkataraman, H. Huang, S.E. Harvey, D.L. Kohlstedt : 1995, vol. 43, pp. 1569-1576.
- [47] D.E. Kramer, K.B. Yoder, W.W. Gerberich : *Philos. Mag. A.*, 2001, vol.

81, pp. 2033-2058.

[48] W.C. Oliver, G.M. Pharr : J. Mater. Res., 1992, vol. 7, pp. 1564-1583.

Chapter 5

General conclusions

The response of a material to the nanoindentation is usually represented as a form of the load-displacement curve. The origin of nanoindentation pop-in, a sudden displacement excursion during load-controlled indentation, is geometrical softening of a test material under the indenter. There can be many reasons for geometrical softening, but among them, investigation of pop-in has mainly been focused on describing it as the elastic-to-plastic deformation transition of metallic materials, based on a Hertzian analysis of the elastic portion of the load-displacement curve. However, other microstructural or crystallographic changes can be the origin of geometrical softening as well. In this study, several physical events which cause pop-ins during nanoindentation of steel were reported and discussed.

First, experimental results of nanoindentation and microstructural studies of metastable austenite in TRIP steel is reported to provide its micromechanical insight into the strain-induced phase transformation and deformation behavior. The load-displacement curve obtained from nanoindentation revealed two types of pop-in events on the loading segment. The first type was attributed to the elastic-to-plastic transition of austenite

based on a Hertzian analysis of the elastic portion of the load-displacement curve. A second type of pop-in can be described as resulting from geometrical softening due to the selection of a favorable martensite variant based on the mechanical interaction energy between the externally applied stress and lattice deformation during nanoindentation. The existence of martensite after nanoindentation was confirmed by TEM analysis of the cross-section of an indented sample. The TRIP strain calculated by simple considering of crystal geometry change during phase transformation was in good agreement with the measured pop-in depth. Multiple pop-ins in less stable austenite was considered as a result of sequentially transformed multiple martensite from austenite.

Second, nanoindentation and microstructural studies are reported to provide experimental evidence of the relationship between the formation of ϵ martensite and pop-in behavior in metastable austenite in high nitrogen TRIP steel. The load-displacement curve obtained from nanoindentation revealed stepwise pop-ins in the early stage of plastic deformation. Considering that the stress-induced ϵ martensite transformation is the predominant deformation mode in the early stage of plastic deformation and its monopartial nature as well, geometrical softening can also occur by ϵ martensite formation. From analyses of high resolution TEM images, a cluster of banded structure under the indent turned out a juxtaposition of (111) planes of γ austenite and (0001) planes of ϵ martensite. The most favorable slip system predicted by simple

calculations based on the Schmid's law was the same one that experimentally observed by TEM. It was also calculated that formation of more than just 10 single ϵ martensite layers in this slip system can introduce several nanometers of pop-in. These microstructural investigations strongly suggest that the pop-in behavior in the early stage of plastic deformation of austenite is closely related to the formation of ϵ martensite.

Lastly, pop-ins on nanoindentation load–displacement curves of a ferritic steel were correlated with yield drops on its tensile stress–strain curves. To investigate the relationship between these two phenomena, nanoindentation and tensile tests were performed on annealed specimens, prestrained specimens, and specimens aged for various times after prestraining. Clear nanoindentation pop-ins were observed on annealed specimens, which disappeared when specimens were indented right after the prestrain, but reappeared to varying degrees after strain aging. Yield drops in tensile tests showed similar disappearance and appearance, indicating that the two phenomena, at the nano- and macroscale, respectively, are closely related and influenced by dislocation locking by solutes (Cottrell atmospheres).

In conclusion, experimental evidences of close relationship between pop-in and several physical events during nanoindentation of steel were investigated. Three different types of steel were used to examine mechanically induced martensitic transformation (α') and epsilon martensite formation (ϵ) from austenite, and breaking and recovery of Cottrell atmosphere in ferrite

during nanoindentation, respectively. Although the mechanisms of them were quite different in each case, the key for pop-in was geometrical softening by sudden lattice movement. From this study, more profound understanding on nanoindentation pop-in and plastic behavior of crystalline materials was achieved.

국문 초록

나노인덴테이션은 재료의 미세 물성 및 기계적 거동을 효과적으로 측정할 수 있는 방법으로, 나노인덴테이션에 대한 재료의 반응은 일반적으로 힘-변위 곡선으로 표현된다. 힘-변위 곡선은 주로 연속적인 곡선의 형태이지만, 나노인덴테이션 중에 재료 내부에서 전위 생성, 전위 활성화, 상변태, 변형쌍정 등의 특수한 물리적 변화가 기하학적 연화 현상을 동반하여 발생할 경우 불연속적 거동이 곡선 상에 나타나기도 한다. 이러한 불연속 거동은 가압 속도가 일정할 경우 갑작스러운 변위의 증가로 나타나며, 이를 나노인덴테이션 pop-in 현상이라고 한다. 나노인덴테이션 pop-in 현상의 원인 중에서 가장 잘 알려진 것은 탄성 변형에서 소성 변형으로의 전이, 즉 항복 현상으로, 지금까지 다양한 재료에 대하여 다양한 방법으로 깊이 있는 연구가 이루어져 왔다. 그러나 기하학적 연화 현상의 원인이 될 수 있는 다른 원인들에 대해서는 많은 연구가 이루어지지 않았다. 따라서 본 고에서는 철강 재료를 이용하여 금속 재료에서 일어날 수 있는 pop-in의 다양한 원인을 실험적인 방법으로 제시하였다.

먼저, 변태소성강의 준안정 오스테나이트상의 나노인덴테이션

거동을 측정하였다. EBSD, SEM, SPM, FIB, TEM 등의 분석 장비들을 연계 활용하여 미세조직 기반의 해석을 수행할 수 있었다. 오스테나이트의 나노인덴테이션 시 두 가지 종류의 pop-in이 나타났는데, 첫 번째는 항복 현상에 의한 것이었으며, 두 번째는 변형 유기 마르텐사이트 변태로 인해 발생하는 기하학적 연화에 의한 것으로 설명할 수 있었다. Pop-in 발생 이후 마르텐사이트의 생성 여부는 압흔 종단면의 TEM 관찰을 통해 확인할 수 있었다.

다음으로, ϵ -마르텐사이트 형성이 초기 변형 기구로 작용하는 강재의 나노인덴테이션 거동을 측정하였다. 이 경우, 항복 지점에서 계단식 pop-in이 측정되었다. 응력 유기 ϵ -마르텐사이트는 부분 전위가 한 방향으로만 발생한다고 알려져 있는데, 인덴테이션 아래 부분을 HRTEM으로 관찰하여 이를 확인할 수 있었다. 결정 방위를 고려하면 약 열 개 이상의 ϵ -마르텐사이트 층이 같은 방향으로 생성될 경우 측정된 pop-in과 같은 거동을 일으킬 수 있는 것으로 예상되는데, 이는 측정 결과와 일치하였다.

마지막으로, 페라이트강을 이용하여 항복점 현상과 pop-in과의 관계를 살펴보았다. 먼저 인장 시험을 통해 재료의 항복점 현상 및 변형 시효 거동을 확인하였다. 나노인덴테이션 시에는 항복 지점에서 매우 큰 pop-in이 측정되었다. 그러나 6%의 변형을 가한

시편에서는 pop-in이 발생하지 않았고, 시간이 지날수록 pop-in이 회복되는 경향을 보였다. 이는 인장 시험에서 측정된 항복점 현상 및 변형 시효 효과와 일치하는 결과이며, 이로써 체심입방구조인 페라이트에서 나타나는 나노인덴테이션 pop-in은 항복점 현상과 깊은 관련이 있음을 밝혀내었다.

핵심어: 나노인덴테이션, Pop-in, 기하학적 연화, 변형 유기 마르텐사이트 변태, ϵ -마르텐사이트, 준안정 오스테나이트, 변태소성강, 항복점 현상, Cottrell 분위기, 나노인텐터, 전자후방산란회절, 주사탐침현미경, 집속이온빔, 투과전자현미경

Student number: 2007-20720